Advanced Atomic Layer Deposition Techniques for Metal-Insulator-Metal Diodes

by

Abdullah Alshehri

A thesis
presented to the University of Waterloo
in fulfillment of the
thesis requirement for the degree of
Masters of Applied Science
in
Mechanical and Mechatronics Engineering (Nanotechnology)

Waterloo, Ontario, Canada, 2017

©Abdullah Alshehri 2017

AUTHOR'S DECLARATION

I hereby declare that I am the sole author of this thesis. This is a true copy of the thesis, including any required final revisions, as accepted by my examiners.

I understand that my thesis may be made electronically available to the public.

Abstract

Metal-Insulator-Metal (MIM) diodes are nanoelectronic devices that operate by quantum tunneling of electrons through a thin dielectric layer to rectify high frequency alternating current (AC) to usable direct current (DC). In this research, two fabrication techniques are explored to improve the MIM diode fabrication process; the introduction of a thickness gradient and doping of the insulator layer.

Atmospheric pressure spatial atomic layer deposition (AP-SALD) is used for the first time for the combinatorial fabrication of MIM diodes. This unique technique is used to deposit thin dielectric films with a thickness gradient. A plasma-assisted atomic layer deposition (PAALD) technique is utilized for deposition of nitrogen-doped TiO_2 films. Tuning the electron affinity (χ) of the insulator by doping is expected to improve the rectification of the diode.

Pt-Al_2O_3-Al diodes have been fabricated by AP-SALD to demonstrate the capability of this method for rapid, scalable and atmospheric insulator layer deposition. Current-voltage measurements of these diodes exhibit high asymmetry and nonlinearity. In addition, AP-SALD was implemented to fabricate combinatorial and high-throughput Pl-Al_2O_3-Al diodes via the introduction of an Al_2O_3 thickness gradient. Current-voltage characteristics and figures of merit (FOM) for the MIM diodes show variations with the thickness gradient of the Al_2O_3 insulator.

A plasma assisted atomic layer deposition (PAALD) system was used to deposit nitrogen-doped titanium dioxide. A simple approach was developed that requires only a nitrogen plasma and short plasma exposure times to effectively dope TiO_2. A range of nitrogen dopant concentrations were achieved by varying the flow rate and exposure times of nitrogen and oxygen plasmas. A nitrogen content as high as 27.2±0.5 at. % was observed when only the nitrogen plasma was used. The type of nitrogen doping can be varied from purely substitutional to entirely interstitial, as measured by X-ray photoelectron spectroscopy (XPS). UV-Visible spectroscopy measurements showed a shifting in the

absorption edge from 350 to 520nm with doping, indicating band gap narrowing from 3.1eV to 1.8eV.

Acknowledgements

I would like to express my special thanks to my great supervisors Prof. Mustafa Yavuz and Prof. Kevin Musselman for their support, patience, and guidance during my study to obtain master's degree.

I also thank my groupmates especially Dawood Alsaedi, Khaled Ibrahim and Kissan Mistry, for their help to complete this work. Special appreciations for all my friends in Canada especially, Faisal Aldawsari, Nizar Alshrief and Mohammed Fekri for their advice.

I would like to thank Professor Norman.Y Zhou and Professor Adam Wei Tsen for being the readers of my thesis.

I am also grateful to Dr. David Muñoz-Rojas, and Viet Huong Nguyen from University Grenoble Alpes - CNRS, Grenoble, France for their collaboration on AP-SALD that enabled part of this work.

Furthermore, I would like to thank Sattam bin Abdulaziz University and Saudi Arabian Cultural Bureau for supporting me financially during my journey.

Dedication

To my father: Hamoud

To my mother: Fatima

To my wife: Amjad

To my brothers: Mohammed, Hassan, Fares, Osama and Qasem

To my sister: Afaf

To my best friend: Mayed Ayed Alshehri

Table of Contents

AUTHOR'S DECLARATION....................ii

Abstract....................iii

Acknowledgements....................v

Dedication....................vi

Table of Contents....................vii

List of Figures....................ix

List of Tables....................ix

List of Abbreviations....................xii

Chapter 1 Introduction....................1

1.1 Background....................1

1.2 Metal Insulator Metal (MIM) Diode....................3

1.2.1 Principle of Operation....................3

1.2.2 DC Characteristics and Figures of Merit (FOM) of MIM Diode....................5

1.2.3 State of the art....................8

1.3 Objectives....................9

1.4 Atmospheric Pressure Spatial Atomic Layer Deposition (AP-SALD)....................10

1.5 Combinatorial techniques....................11

1.6 Titanium Dioxide (TiO_2) Doping....................12

Chapter 2 MIM Diodes by Atmospheric Pressure Spatial Atomic Layer Deposition (AP-SALD)....................14

2.1 Experimental....................14

2.1.1 Sample preparation....................14

2.1.2 Photoresist Coating....................14

2.1.3 Photolithography....................15

2.1.4 Development of Photoresist....................16

2.1.5 Metals Deposition (First Metal)....................16

2.1.6 First Lift off process....................17

2.1.7 Dielectric Thin Film Deposition....................17

2.1.8 Second photoresist coating, photolithography, deposition and lift off.....................19

2.1.9 Dry Etching....................20

2.2 Results and Discussion....................21

Chapter 3 Combinatorial MIM Diodes Studies....................25

3.1 Experimental.........25
3.2 Results and Discussion.........27
Chapter 4 Nitrogen Doping Titanium Dioxide (N Doping TiO_2) by PAALD.........30
4.1 Objective.........30
4.2 PAALD of N-Doped TiO_2.........31
4.2.1 Characterization of N -Doped TiO_2.........33
4.3 Result and Discussion.........33
Chapter 5 Conclusion and Future work.........45
Bibliography.........46

List of Figures

Figure 1.1. Block diagram of rectenna device [2]. 2
Figure 1.2 Energy diagram of MIM Diode 4
Figure 1.3. Energy band diagrams of a MIM diode for (a) unbiased, (b) low negative bias, (c) high negative bias, (d) low positive bias, and (e) high positive bias conditions. 5
Figure 1.4 (a) A schematic diagram of AP-SALD with various precursors. (b) Precursor A is pulsing when the substrate oscillates underneath it to absorb a monolayer. After that, the substrate oscillates underneath inert gas (I) to purge un-reacted precursor A. (c) Precursor B is pulsing when the substrate oscillates underneath it to grow a desired layer 11
Figure 2.1 (a) Mask 1 (b) Mask 2 (c) Combination of Masks 1&2[39]. (d) The Karl Suss MA6 Aligner. 16
Figure 2.2: The Intlvac Nanochrome e-beam evaporator 17
Figure 2.3 (a) Schematic of principle to carry precursor from liquid bubbler to gas liquid (b) Al_2O_3 deposition by AP-SALD. 18
Figure 2.4 Thickness of Al_2O_3 film vs Substrate oscillation. 19
Figure 2.5 Summary of fabrication process of Pt/Al_2O_3/Al diode using AP-SALD. 20
Figure 2.6 Fabricated MIM diodes. The diode with smallest contact area (labelled 10, which means 10 μm x 10 μm) is measured in this work. 21
Figure 2.7 Schematic diagram of MIM diode characterization system. 22
Figure 2.8 I-V characteristics of the Pl-Al_2O_3-Al diodes. (a) I-V curve. (b) Asymmetry with voltage. (c) Nonlinearity with voltage. (d) Responsivity with voltage. 23
Figure 3.1 A schematic illustration of thickness gradient Al_2O_3 film deposition by AP-SALD. 26
Figure 3.2 Thickness gradient MIM diode architecture 26
Figure 3.3 Measurement of thickness gradient across an Al_2O_3 film using AFM. 28
Figure 3.4 I-V curves of different Al_2O_3 thickness for Pt/Al_2O_3/Al diodes: (a) 8.5 ±1.9 nm (b) 6 ±1.9 nm (c) 2.4 ±0.2 nm. Figures of merit for 18 different Al_2O_3 diode thicknesses are calculated and plotted in (d), (e), (f) as asymmetry, nonlinearity, and responsivity respectively. 29
Figure 4.1. Flow chart of PAALD cycle developed in this work and cycle reported in previous work[33]. Recipes that produced the highest nitrogen contents are shown 32
Figure 4.2 (a) UV-vis spectra of TiO_2 and N- doped TiO_2 films (b) Tauc plotting of UV-vis spectra of TiO_2 and N- doped TiO_2 films 34

Figure 4.3: Ti 2p XPS spectra of TiO_2 and N-doped TiO_2 films: (a) TiO_2 (b) 3s O_2/N_2 plasmas (c) 1s N_2 plasma (d) 3s N_2 plasma (e) 5s N_2 plasma (f) 7s N_2 plasma. 36
Figure 4.4: Ti^{4+} and Ti^{3+} peak intensities for increasing nitrogen plasma exposure. 37
Figure 4.5: N1s XPS spectra of TiO_2 and N-doped TiO_2 films: (a) TiO_2 (b) 3s O_2/N_2 plasmas (c) 1s N plasma (d) 3s N plasma (e) 5s N plasma (f) 7s N plasma. 41
Figure 4.6. O1s XPS spectra of TiO_2 and N-doped TiO_2 films: (a) TiO_2 (b) 3s N............................. 42

List of Tables

Table 1. The MA6 exposure parameters for photolithography method. 15

Table 2: Al_2O_3 deposition conditions by AP-SALD.. 19

Table 3. Previous reported work for Al-Al_2O_3-Pt diode. 24

Table 4: Process recipes for PAALD films. 32

Table 5: Literature Data on the XPS binding energies (eV) of Ti 2p, N 1s, and O 1s[55]. 43

Table 6: Film compositions of PAALD samples. 44

List of Abbreviations

MIM	Metal-Insulator-Metal
CHT	Combinatorial High Throughput
ALD	Atomic layer deposition
PAALD	Plasma Assisted Atomic Layer Deposition
AP-SALD	Atmospheric Pressure Spatial Atomic Layer Deposition
EBV	Electron Beam Evaporator
RIE	Reactive Ion Etching
AFM	Atomic Force Microscopy
UV-vis	Ultraviolet- visible
XPS	X-ray Photoemission Spectroscopy
MA6	Mask Aligner
RF	Radio frequency
IR	Infrared
PV	Photovoltaic
AC	Alternative Current
DC	Direct Current
GPC	Growth Per Cycle
TIIP	Titanium isopropoxide
THz	Terahertz
FOM	Figure of merit
TOV	Turn on voltage
FN or FNT	Fowler Nordheim tunneling

Chapter 1
Introduction

1.1 Background

The global demand for energy as well as its applications in our lives continue to increase and thus it has become important to find alternative sources of green and economical energy to eliminate the use of fossil fuels due to the high cost and negative environmental effects. In recent years, researchers have worked on improving the renewable energy technologies that depend on several natural resources such as wind and solar. Solar cells are energy harvesting devices that convert visible sunlight into useable electricity. However, the semiconductor band gap limits solar cell efficiency, thus alternative solar energy harvesting technology with high efficiency is of interest. Brown, W.C. in 1964, demonstrated the rectifying antenna as an alternative to traditional solar cells also the rectenna can works as harvester device in different energy regime from IR to UV when the cut off frequency of the rectifier diode is in range of 10^{12} - 10^{15} while the RC constant of the diode is in femtosecond range [1] .The rectenna (RECTifying antENNA) is a

photoelectronic device consisting of two major components: a nanoantenna and a rectifier diode, as shown in Figure 1.1. The rectenna device is capable of converting sunlight into useable electrical power.

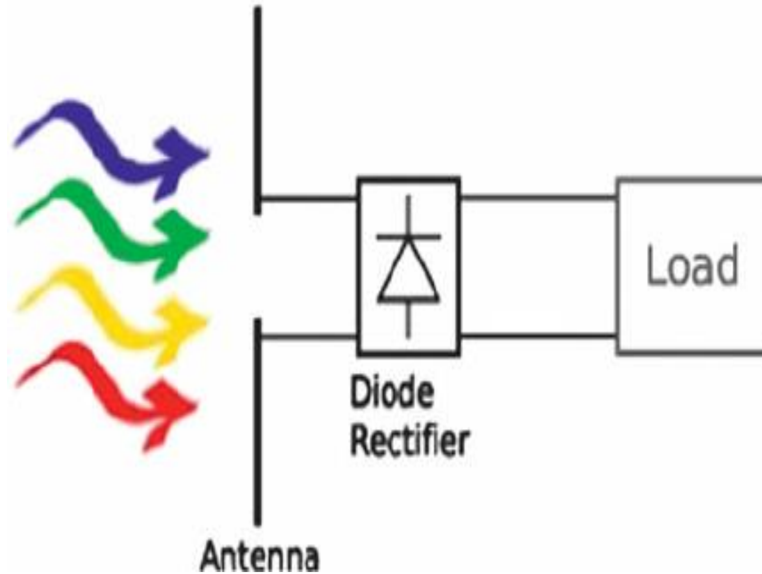

Figure 1.1. Block diagram of rectenna device [2].

Electromagnetic waves (GHz or THz range) captured by the nanoantenna are converted to an alternating current (AC) and subsequently rectified to usable direct current (DC) transferred to a load. A rectifier diode in the rectenna system plays an important role to improve the conversion efficiency of electromagnetic waves into electricity. In order to harvest more energy, a rectenna that works at high frequencies is needed because of the frequency of the visible light spectrum. Schottky diodes are popular rectifying devices based on a semiconductor-metal junction, but are limited to GHz or low THz frequency applications such as IR detectors [3]. For solar energy harvesting, rectifier diodes that operate in the high THz range are needed to rectify high frequency current that is received from the antenna. Metal Insulator Metal (MIM) diodes are capable of rectification in the high frequency range because they are based on a femtosecond electron transport mechanism through the insulator. Thus the MIM diode is attractive for

many applications such as solar rectennas [3], memory switching devices[4], field emission cathodes[5], and LED displays[6].

1.2 Metal Insulator Metal (MIM) Diode

A MIM diode is a nonlinear nanoelectronic device consisting of a thin dielectric layer stacked between two metal contacts. Conduction in the diode occurs via electron tunneling between the two metals through the dielectric layer. Rectification is achieved as a result of the asymmetry of the two potential barriers formed between the metals and the insulator, which influences the electron tunneling rates. While the electrons tunnel to overcome the potential barriers, the tunneling probability is reduced by the barrier. A larger potential barrier at one metal-insulator interface results in a larger reduction in the tunneling probability than at the other metal-insulator interface. The design of the potential barriers therefore has significant impact on MIM diode characteristics such as turn on voltage, asymmetry, nonlinearity, and responsivity (defined in Section 1.2.2).

1.2.1 Principle of Operation

The materials selection of the diode determines its energy diagram and has a significant impact on diode performance, as shown in Figure 1.2. Potential barriers are formed at the interfaces of the metals and the insulator. The barrier height (ψ) is the difference between the work function (ϕ) of the metal and the electron affinity (χ) of the insulator, and the barrier width is defined by the insulator thickness. E_f in Figure 1.2 indicates the Fermi level in the diode.

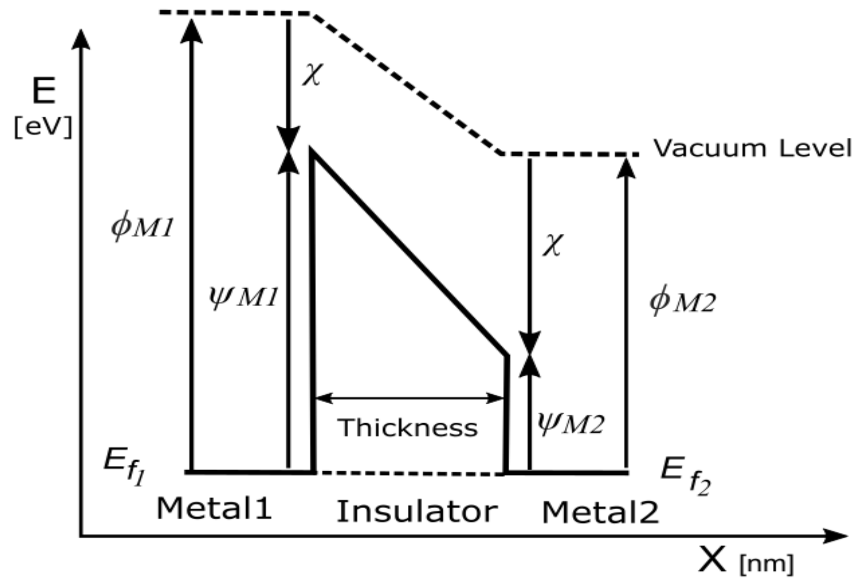

Figure 1.2 Energy diagram of MIM Diode.

Figure 1.3 explains the principle of operation of an MIM diode. Consider a designed MIM diode with different metal electrodes where Metal 2 has a smaller work function than Metal 1. Figure 1.3a, shows the diode in the unbiased condition (V=0), where equilibrating the fermi levels of the two metal contacts forms a trapezoidal barrier atop the potential barrier. Reverse current results when negative bias (V<0) is applied to metal 2 and the band diagram has a small shift in its shape due to raising of the fermi level of metal 2, as shown in Figure 1.3b. In this configuration, the electrons must tunnel through the entire dielectric thickness (d_t). A further increase in negative bias (V<<0) results in a change in the trapezoidal barrier to a triangular barrier, allowing Fowler-Nordheim (FN) tunneling to occur which is the process related to increase the probability of electron tunneling through the triangular barrier benefiting from reduced tunneling distance that formed atop of the barrier because of the difference in work functions of metals ($\Delta\phi$) and applied voltage (V), thus the probability of FN tunneling is increased with high values of asymmetric ratio of MIM diodes as shown in Figure 1.3c. Forward bias occurs when a low positive bias is applied to metal 2 (V>0), so that FN tunneling takes place and the tunneling distance is reduced, as shown

in Figure 1.3d. A further increase in positive bias will decrease the tunneling distance further and consequently the tunneling current density will increase, as in Figure 1.3e. The diode's rectification capability follows from the reduced tunneling distance in the forward direction that encourages electron tunneling in the forward bias, as compared to the limited reverse bias current at the same voltage magnitude.

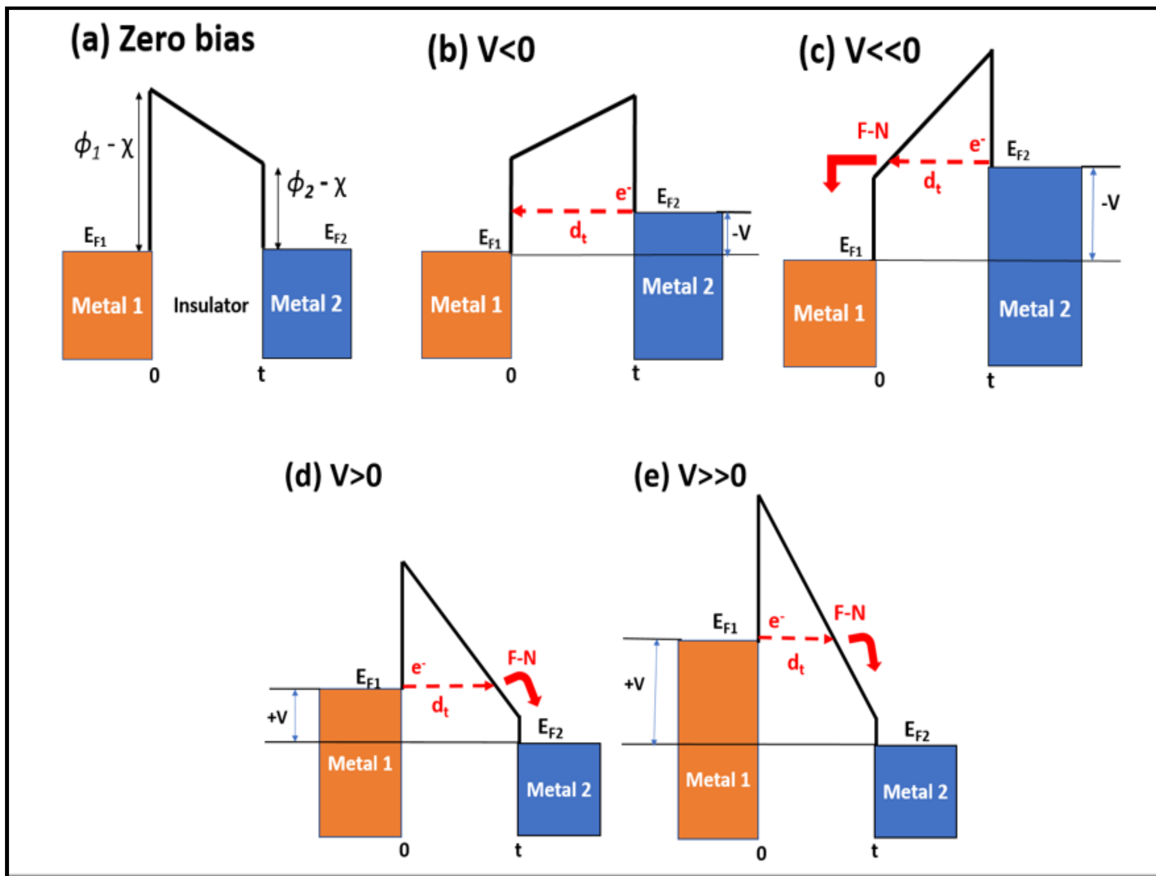

Figure 1.3. Energy band diagrams of a MIM diode for (a) unbiased, (b) low negative bias, (c) high negative bias, (d) low positive bias, and (e) high positive bias conditions.

1.2.2 DC Characteristics and Figures of Merit (FOM) of MIM Diode

Rectification performance of MIM diodes is characterized by three parameters known as the diode Figures of Merit (FOM): asymmetry, nonlinearity, and responsivity. These figures of merit are affected

by several factors such as metal and insulator selection, insulator thickness, and barrier height between metal and insulator.

1.2.2.1 Current-Voltage (I-V) Curve:

The Current-Voltage (I-V) curve of a MIM diode describes several characteristics of the diode such as current density, turn on voltage, and resistivity. In addition, the figures of merit (asymmetry, nonlinearity, and responsivity) are determined from the I-V curve.

1.2.2.2 Asymmetry

Asymmetry is the absolute ratio of forward to reverse current at a voltage and can be calculated from equation (1-1), where a value larger than 1 indicates rectification in the diode. The work function of the metal electrodes play a significant role in the asymmetric behavior of MIM diodes. Electrodes of the same metal are expected to result in a symmetric I-V curve. A high asymmetric diode requires dissimilar electrodes with a work function difference greater than 30meV[7]. In addition, MIM diodes show increasing asymmetry with insulator thickness[8].

$$Asy = \left| \frac{I_F(V)}{I_R\ (V)} \right| \tag{1-1}$$

Where I_F is the forward current and I_R is a reverse current at a voltage V.

1.2.2.3 Nonlinearity

Nonlinearity is a measure the degree of variation from a linear I-V curve. It is the ratio of the slope of the I-V curve to the conductance at a bias, as shown in equation (1-2). Nonlinearity increases with insulator

thickness[8] and low barrier height when the work function (ϕ) value of one metal is around the electron affinity of the dielectric [7].

$$NL = \frac{\frac{dI(v)}{dV}}{\frac{I(v)}{V}} \tag{1-2}$$

1.2.2.4 Responsivity

Responsivity is a measure of the ability of an MIM diode to generate DC current per input of AC electrical power. It is defined in equation (1-3) as the ratio of the second derivative to the first derivative of the I-V curve at a bias.

$$Res = \frac{d^2 I(v)}{d^2 V} / \frac{dI(v)}{dV} \tag{1-3}$$

1.2.2.5 Other Characteristics

Other parameters must also be taken into consideration when designing and characterizing an MIM diode. The cut off frequency f_c, for example, is the theoretical maximum rectified frequency that can be achieved by an MIM diode. High cut off frequency is required with small resistance and capacitance, as in Eq (1-4)[9]

$$f_c = \frac{1}{2\pi RC} \tag{1-4}$$

Where R is the series resistance of the MIM diode with coupled devices such as an antenna; C is the diode capacitance and can be measured by Eq (1-5):

$$C = \varepsilon_0 \varepsilon_r \frac{A}{d} \tag{1-5}$$

Where ε_0 is the permittivity of free space, ε_r is the relative permittivity or dielectric constant of the insulator, A is the contact area of the diode, and d is the insulator thickness.

1.2.3 State of the art

Design and fabrication of MIM diodes is the most significant topic in the MIM diode research area. In this literature review, the dielectric layer in the MIM stack plays a significant role in the diode performance. Several methods have been reported for the deposition of the insulator layer such as sputtering[10], physical vapor deposition(PVD)[11], anodic oxidation of sputtered films[12], Langmuir Blodgett technique[13] and atomic layer deposition (ALD)[14].

Abdel-Rahman et al. fabricated an MIM diode with a novel diode material combination: Cu-CuO-Cu [10]. The copper metal was deposited by RF sputtering and patterned by electron beam lithography then the copper oxide was deposited by RF sputtering. Their MIM diode showed a responsivity of 4.497A/W.

Ozkan, E. G. et al. designed and developed 3 different MIM diodes: Au-Al_2O_3-Al, Au-Cr_2O_3-Cr, Au-TiO_2-Ti for infrared detection and energy harvesting applications. The physical vapor deposition (PVD) fabrication process was optimized for the MIM diodes and they achieved high responsivity and nonlinearity of 15 A/W and 80 respectively for the Au-Al_2O_3-Al diode[11].

Periasamy, P. et al. studied the influence of the metal work function difference on MIM diode performance. Their diode structure had Niobium (Nb) as the bottom contact and a Niobium Oxide (Nb_2O_5) insulator layer deposited by anodic oxidation technique. The metal top contact was a bent wire of 8 different metals, thus this method showed rapid fabrication and sequential characterization of the MIM diodes. The difference between work functions of the two metals had a significant impact on rectification performance of the diodes, where asymmetry increased with work function difference and the nonlinearity showed a non-monotonic relation. The best FOMs were achieved for Nb-Nb_2O_5-Pt

combination, where 1500, 4, and 20A/W are obtained for asymmetry, nonlinearity and responsivity, respectively[12].

Sharma et al. used an atmospheric pressure technique to fabricate an MIM diode. The Langmuir-Blodgett method, where an air-water interface is used to deposit a monolayer of a material at the liquid surface by immersion of the substrate into the liquid, was used to deposit 10,12-pentacosadiynoic acid (PDA) as an insulator layer stacked between two Ni metal electrodes. The work shows accurate thickness control of the PDA monolayer and the I-V diode characteristic shows tunneling behavior with an asymmetry of 110 at ± 200 mV[13].

A scalable and precise thin film deposition techniques is atomic layer deposition (ALD). This method can produce a smooth and uniform film, which is attractive for fabricating MIM diodes. Alimardani et al. studied the rectification behavior and the (I-V) characteristics of MIM diodes at different temperature ranges. Furthermore, the conduction mechanisms at low and high biases were measured. Atomic layer deposition was used to grow Nb_2O_5 and Ta_2O_5 as insulators in MIM diodes, and the metals were ZrCuAlNi and Al deposited by DC magnetron sputtering. Alimardani et al. found that the Schottky emissions are dominant for both insulators at small biases and Frenkel–Poole emission at high biases, while FN tunneling had no influence on I-V asymmetry determination[14].

1.3 Objectives

The main objective of this research is to investigate a new scalable fabrication technique for MIM diodes. Atmospheric pressure spatial atomic layer deposition (AP-SALD) is introduced for the first time to fabricate an MIM diode.

Another objective is optimizing fabrication and characterization of an MIM diode by using a combinatorial and high throughput technique, by the introduction of a thickness gradient to optimize the

device. This allows the study of several insulator thicknesses at once. A novel combinatorial technique for AP-SALD is used and applied to fabricate a high throughput MIM diode.

A further goal of this research is improving rectification performance of MIM diodes. Tuning the electron affinity of the insulator by doping appears promising for improving MIM diode performance. MIM diodes have shown improvement in rectification performance at a small potential barrier when the electron affinity of the insulator is close to the work function of the metal [7]. Nitrogen doped TiO_2 is produced *via* plasma assisted atomic layer deposition (PAALD) with a high nitrogen concentration of 27.2±0.5 at%, which will enable tuning of the electron affinity of the insulator layer.

1.4 Atmospheric Pressure Spatial Atomic Layer Deposition (AP-SALD)

Atmospheric pressure spatial atomic layer deposition (AP-SALD) is a fast and scalable thin film deposition technique that operates in atmospheric pressure. It has the ability to control the film thickness in the atomic scale range and produce uniform and pinhole-free films at modest temperatures (e.g. 80-200 °C). [15]. Figure 1.4 illustrates the working principle of AP-SALD: the system has two precursors separated by an inert gas. The inert gas is bubbled through the precursors to evaporate them and enable the precursor delivery. The substrate is placed under the atmospheric gas manifold with a small vertical separation (bellow 100μm) to expose the substrate to the alternating precursors. To grow a monolayer, the substrate oscillates underneath the first precursor (A) to absorb the first layer of the precursor, then the substrate moves under the flow of inert gas (I) to remove remaining precursor A in the gas phase, as shown in Figure 1.4b, then the monolayer is completed when the substrate moves under precursor B to react with the layer of precursor A, as in Figure 1.4c. By repeating this cycle with oscillations of the substrate back and forth, the desired scalable thickness can be grown as a high-quality, pinhole-free film.

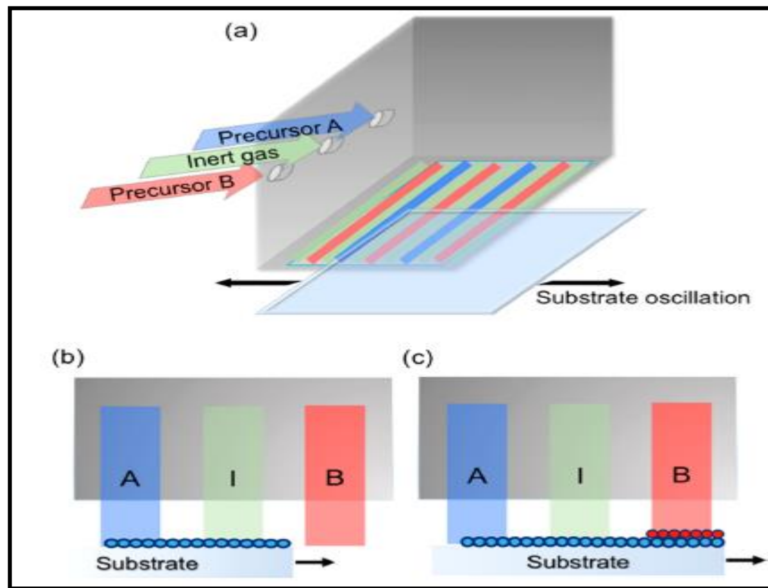

Figure 1.4 (a) A schematic diagram of AP-SALD with various precursors. (b) Precursor A is pulsing when the substrate oscillates underneath it to absorb a monolayer. After that, the substrate oscillates underneath inert gas (I) to purge un-reacted precursor A. (c) Precursor B is pulsing when the substrate oscillates underneath it to grow a desired layer

1.5 Combinatorial techniques

Combinatorial High Throughput (CHT) experimentation technologies have the capability to discover and optimize new materials by producing large arrays of diverse materials together to map the materials' properties. Experimental artifacts that result from uncontrolled differences in experimental conditions can be eliminated using CHT techniques to get better data than by conventional approaches that require iteration of the material synthesis process[16]. Materials are being developed by CHT experiments for use in different areas such as electrochemical catalysis, electronics, sensors, and biomaterials[16].

CHT techniques have largely focused on the synthesis of material libraries on one substrate by vacuum-based techniques. RF magnetron co-sputtering[17], for example, was used to produce electrical conductivity and Seebeck coefficient maps of Ce-Co-Sn ternary composition. An electron beam evaporator was utilized to fabricate Fe-Cr-Ni alloys to determine their ternary phase diagram[18], pulsed

laser deposition was used to fabricate thin SnO_2 films with various dopant concentrations for gas sensors[19], and chemical vapor deposition CVD was used to fabricate ZrO_2 or HfO_2 with SiO_2 to identify compositions with high dielectric constant (k)[20]. In terms of atmospheric CHT techniques, Combinatorial Atmospheric CVD (cACVD) and spray pyrolysis have been used to achieve composition and thickness gradients. Yates et al., for example, used cACVD to dope SnO_2 with fluorine for optimum performance in solar cells[21], and Kafizas et al. synthesized a titania film with a thickness map and gradating nitrogen dopant and phase from anatase to anatase–rutile[22]. Pavan et al. used spray pyrolysis to produce TiO_2/Cu_2O heterojunctions with a thickness gradient to optimize solar cell performance[23].

1.6 Titanium Dioxide (TiO_2) Doping

Titanium dioxide (TiO_2) has been used for a variety of applications including sensors[24], photovoltaics[25], and as a photocatalyst for environmental and energy purposes (e.g. self-cleaning surfaces, water and air purification)[22] because it is chemically stable, low cost and abundant. However, the large band gap of the anatase form of TiO_2 (3.1 eV) limits the efficiency of photocatalysis under visible light, and the position of its conduction band influences electron transport in devices such as photovoltaics and metal-insulator-metal diodes. To enhance the photocatalytic efficiency of TiO_2 and improve the current-voltage characteristics of TiO_2 devices[26], nitrogen doping (N-doping) has been used to narrow the band gap and increase visible light absorption. Increasing the nitrogen content in TiO_2 can increase the presence of oxygen vacancies, which are responsible for forming $3d$ states of Ti^{3+} below the conduction band[27]. Various deposition processes have been used to introduce N atoms into the TiO_2 lattice of nanoscale films. These have included, sputtering[28], chemical vapor deposition[29], and atomic layer deposition (ALD)[30]. N-doping of TiO_2 has been typically done by ALD with ammonia (NH_3) gas or ammonia and water[31, 32]. The use of an additional precursor introduces complexity, it can be difficult to control the nitrogen content, and the deposited film can change to TiN at high temperature[33,

34]. Plasma assisted atomic layer deposition (PAALD) is an advantageous method for doping, due to its higher reactivity, low deposition temperature[35], and chemical composition control [33]. However, these efforts resulted in low nitrogen contents, or required complex techniques or relatively long deposition times to obtain high nitrogen content. Zhipeng et al.[36] deposited N-doped TiO_2 by PAALD with $TiCl_4$ and H_2O precursors and N_2 plasma gas, achieving a doping level of 1 at.% of nitrogen. Deng et al.[37] achieved a nitrogen content of 9.4 at. % by alternating thermal (ALD) of TiO_2 and (PAALD) of TiN, but the use of alternating deposition methods required a longer deposition time. Zhang et al.[33] deposited $TiO_{2-x}N_x$ ultrathin films by varying the background gas (O_2 or N_2) during the Ti precursor exposure with a N_2/H_2-fed inductively coupled plasma (ICP). They achieved a significant nitrogen content of 13 at.%, as measured at the surface of the film, and up to 22 at.% in the bulk of the film, using a recipe without oxygen precursor. They inserted N_2 gas for 4s through the ICP dosing line during the Ti precursor exposure, but still only achieved 50% substitutional doping. Additionally, their approach used a long (15s) H_2/N_2 plasma exposure time to achieve these nitrogen contents, which would make the film growth prohibitively slow (up to 30s /cycle). Their approach is detailed schematically in Figure 4.1. The PAALD cycle time is the sum of the Ti precursor dosing time, the Ti purge time, the reactant (O_2/N_2) dose time, and the reactant plasma purge time. Thus, using more reactants and longer exposure times leads to increased purge times and increased cycle times, resulting in slow film growth rates. Furthermore, some of the previous reports of N-doped TiO_2 by PAALD used $TiCl_4$ as the precursor[36], which is undesirable due possible chlorine contamination that may result in undesirable chemical properties [38]. Achieving N-doped TiO_2 with minimal contamination/impurities *via* faster depositions employing few precursors is challenging.

Chapter 2

MIM Diodes by Atmospheric Pressure Spatial Atomic Layer Deposition (AP-SALD)

2.1 Experimental

MIM diodes were fabricated using platinum (Pt) as the bottom electrode and aluminum (Al) as the top electrode, with alumina (Al_2O_3) as the thin dielectric layer between the two metals. The metals are chosen based on their high difference in work function to achieve asymmetric behavior in the I-V curve. Pt has a work function of 5.6 eV and Al has a work function of 4.28 eV. The electron affinity of Al_2O_3 is 2.8 eV. Thus, the Pl-Al_2O_3-Al diodes are expected to form two different barrier heights, $\psi_1 = \phi_{Pt} - \chi_{Al2O3}$, and $\psi_2 = \phi_{Al} - \chi_{Al2O3}$, where $\psi_1 > \psi_2$ as represented in Figure 1.2.

2.1.1 Sample preparation

The substrate consists of a 3 inch SiO_2 wafer (100 orientation), 305 to 355 microns thick with a 5000 Å thermal oxide. The wafer is cleaned sequential in baths of acetone and IPA (isopropanol), and subsequently rinsed with deionized water and dried with N_2. Before photoresist coating, the substrate is coated with HMDS (hexamethyldisilazane) for 25s with a spin speed of 3000 RPM to increase the adhesion of photoresist to the silicon oxide surface.

2.1.2 Photoresist Coating

The negative photoresist, maN-1410 is used because it is suitable for the lift off process, and compatible with the designed photomask. With negative photoresist, the unexposed area is removed from the sample after development. The spin coating is started by dispensing the resist over ¾ of the substrate surface followed by spinning at 500 RPM for 5 seconds with an acceleration of 100 RPM/s. The wafer is further spun at 3000 RPM for 60s with an acceleration of 500 RPM/s. This spin speed results in an approximately

1275 nm thick resist layer (measured by Filmetrics F50-UV). To remove the solvent component in the photoresist, the samples are soft-baked at 100°C for 90 sec.

2.1.3 Photolithography

This technique uses UV light to pattern the micro scale shapes on the photoresist using a designed photo mask. The negative photomask pattern provides different device areas, 10 µm x10 µm, 20 µm x 20µm, and 30 µm x 30 µm as shown in the Figure 2.1. The photomask consists of a glass plate with a patterned chromium film. The photolithography process is applied twice before depositing the metal electrodes. In the first exposure, mask 2 is used to pattern the desired shape on the photoresist. MaN-1410 resist requires a dose of 350 mJ/cm^2 at 365 nm. The Karl Sauss (MA6) Aligner is calibrated to provide 10 mW/cm^2 of UV at 365 nm. The wafer is therefore exposed for 35 seconds. The MA6 exposure parameters are summarized in Table 1.

Table 1. The MA6 exposure parameters for photolithography method.

Alignment Gap	Wedge Error Compensation (WEC) offset	WEC type	Exposure type	Pre-Vacuum	Full Vacuum	Purge Vac:
20 µm	0	Contact	Vacuum	5 seconds	15 seconds	10 seconds

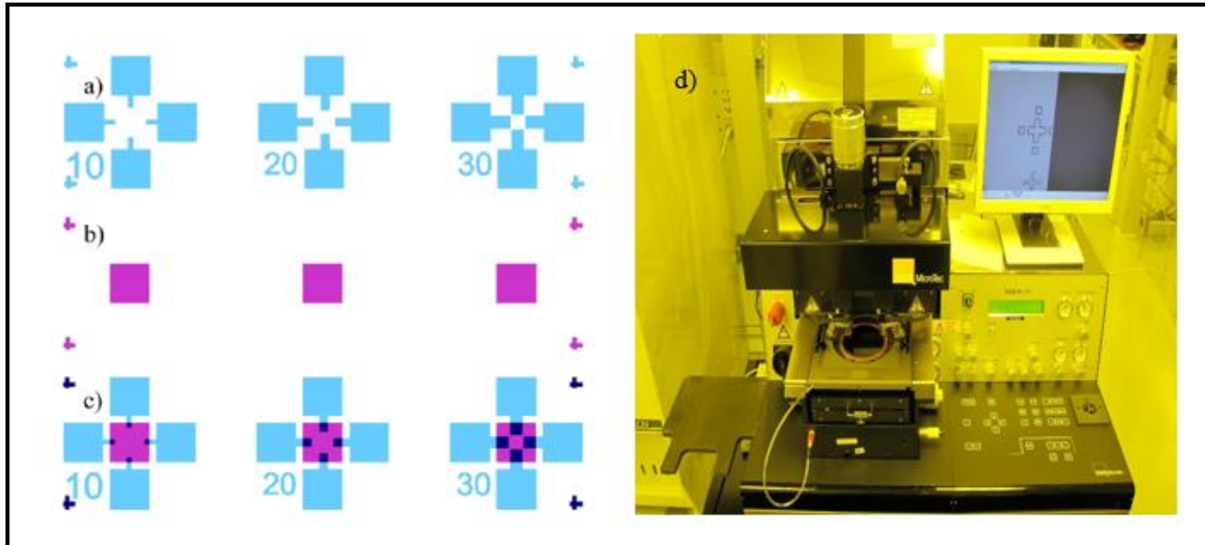

Figure 2.1 (a) Mask 1 (b) Mask 2 (c) Combination of Masks 1&2[39]. (d) The Karl Suss MA6 Aligner.

2.1.4 Development of Photoresist

The development is used to remove unexposed areas of the photoresist. The sample was developed in Ma-D 533/S (tetramethylammonium hydroxide (TMAH) based) and agitated lightly for 120 s at room temperature. After development, the sample was placed in DI water for 1 minute followed by a DI rinse under the water tap and N_2 drying steps. The resolution attained with this recipe is 3.5 µm. The undercut achieved is approximately 2 µm.

2.1.5 Metal Deposition (First Metal)

Platinum (Pt) with 100nm thickness and 1 Å/s deposition rate was deposited on the substrate using an E-beam evaporation (EBV) system shown in Figure 2.2 with a base pressure set to $4x10^{-6}$ torr.

Figure 2.2: The Intlvac Nanochrome e-beam evaporator.

2.1.6 First Lift off process

The lift off method uses a suitable chemical solvent to create structures on a deposited film. In this method, the undesired deposited film is removed with photoresist while the film deposited on the substrate remains.

To lift off the maN-1410 photoresist, the following four process are applied to the sample:

- Sonicate sample in acetone for 5 minutes at 50°C.
- Sonicate sample in Remover PG for 5 minutes at 50°C.
- Sonicate sample in acetone for 5 minutes at 50°C.
- Sonicate sample in isopropanol IPA for 5 minutes at 50°C.
- Blow dry sample with nitrogen.

2.1.7 Dielectric Thin Film Deposition

The insulator film was deposited by AP-SALD. The depositions for this research were performed by collaborators Dr. D. Muñoz-Rojas and V. Nguyen in Grenoble using a custom-built AP-SALD system, where unlike conventional ALD, the substrate moves underneath spatially separated precursor gas flows.

To obtain 8nm thickness of Al_2O_3, the distance between the deposition head and substrate is adjusted to 100µm. In this process, three precursors are used: tetramethylammonia (TMA), H_2O, and N_2 as the inert gas. The process begins with bubbling N_2 gas through the TMA liquid precursor at a flow of 15 sccm, as shown in Figure 2.3a, to aid TMA delivery to the substrate. The N_2 carrier gas (labeled "dilution line" in Figure 2.3a) has a flow of 235 sccm. The substrate moves underneath the TMA precursor flow, as shown in Figure 2.3b, forming a partial monolayer of adsorbed TMA. After that, it moves underneath the N_2 inert gas with a flow of 750 sccm to remove unreacted ligands of TMA before moving underneath the H_2O precursor that flows at 100 sccm to react with the TMA layer to form a monolayer of Al_2O_3 as shown in Figure 2.3b. The substrate oscillation speed is set to 10 cm/s and the oscillation number was 15 , where increasing the oscillation number can change the Al_2O_3 thickness, as shown in Figure 2.4. The Al_2O_3 AP-SALD deposition conditions are summarized in Table 2.

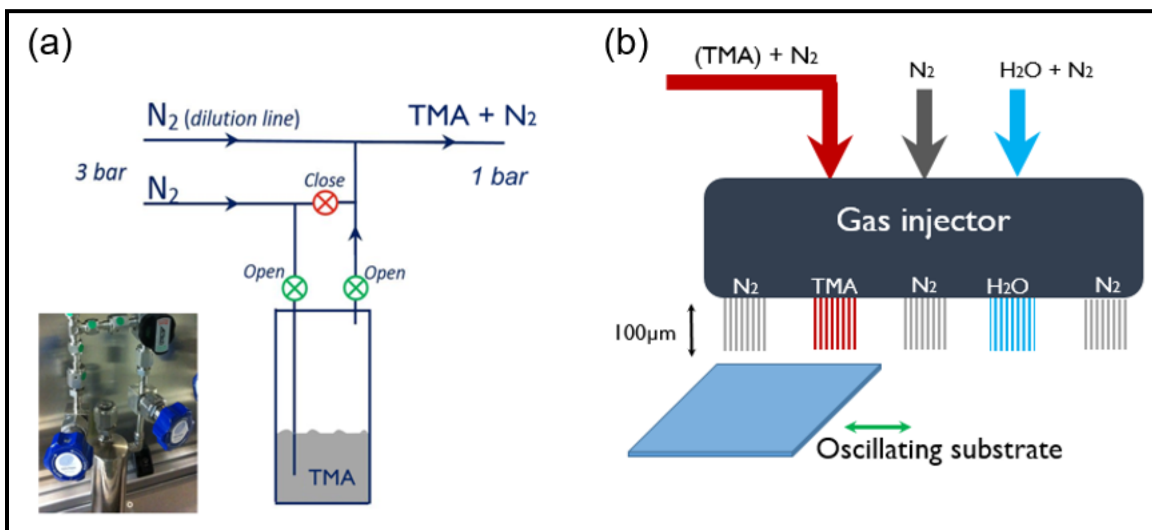

Figure 2.3 (a) Schematic of principle to carry precursor from liquid bubbler to gas liquid (b) Al_2O_3 deposition by AP-SALD.

Table 2: Al_2O_3 deposition conditions by AP-SALD.

Deposition temperature (°C)	Oscillation speed (cm/s)	Distance between injector-substrate (µm)	Gas flows for TMA		Gas flows for H_2O		N_2 rate (sccm)	Flow per channel (sccm)
			Bubbling rate (sccm)	N_2 dilution (sccm)	Bubbling rate (sccm)	N_2 dilution (sccm)		
150	10	100	15	235	100	275	750	125

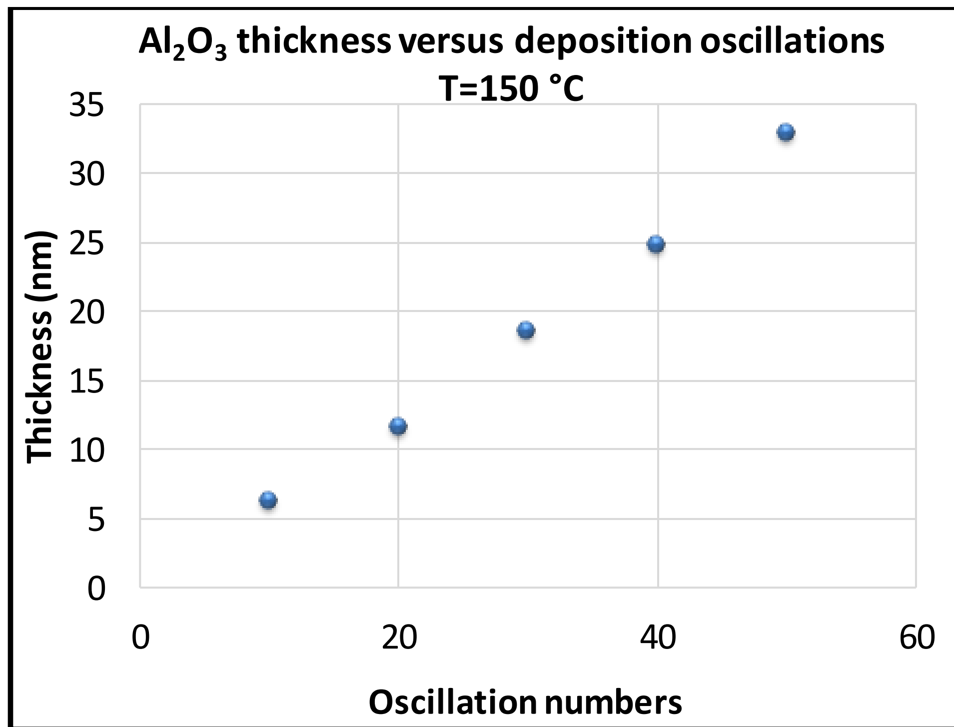

Figure 2.4 Thickness of Al_2O_3 film vs Substrate oscillation.

2.1.8 Second photoresist coating, photolithography, deposition and lift off

To deposit the metal top contact, the same processes that were used to deposit the bottom contact are repeated with a few changes in the second UV exposure and metal deposition. The Pt contact on the sample is aligned with Mask 1 and exposed. Al is deposited as a second contact on top of the insulator

layer. After that, the second lift off process is applied to remove the photoresist to achieve the desired MIM diode.

2.1.9 Dry Etching

The final step of the MIM diode fabrication is dry etching. A Phantom II Reactive Ion Etching (RIE) system is used to bombard the exposed Al_2O_3 in order to remove it and expose the Pt electrode. A flow of Argon plasma (30 sccm) was generated by radio frequency (RF) with a power of 20W for 60s. Figure 2.5 summarizes the MIM diode fabrication process by AP-SALD and a microscopic image of the MIM diodes is shown in Figure 2.6.

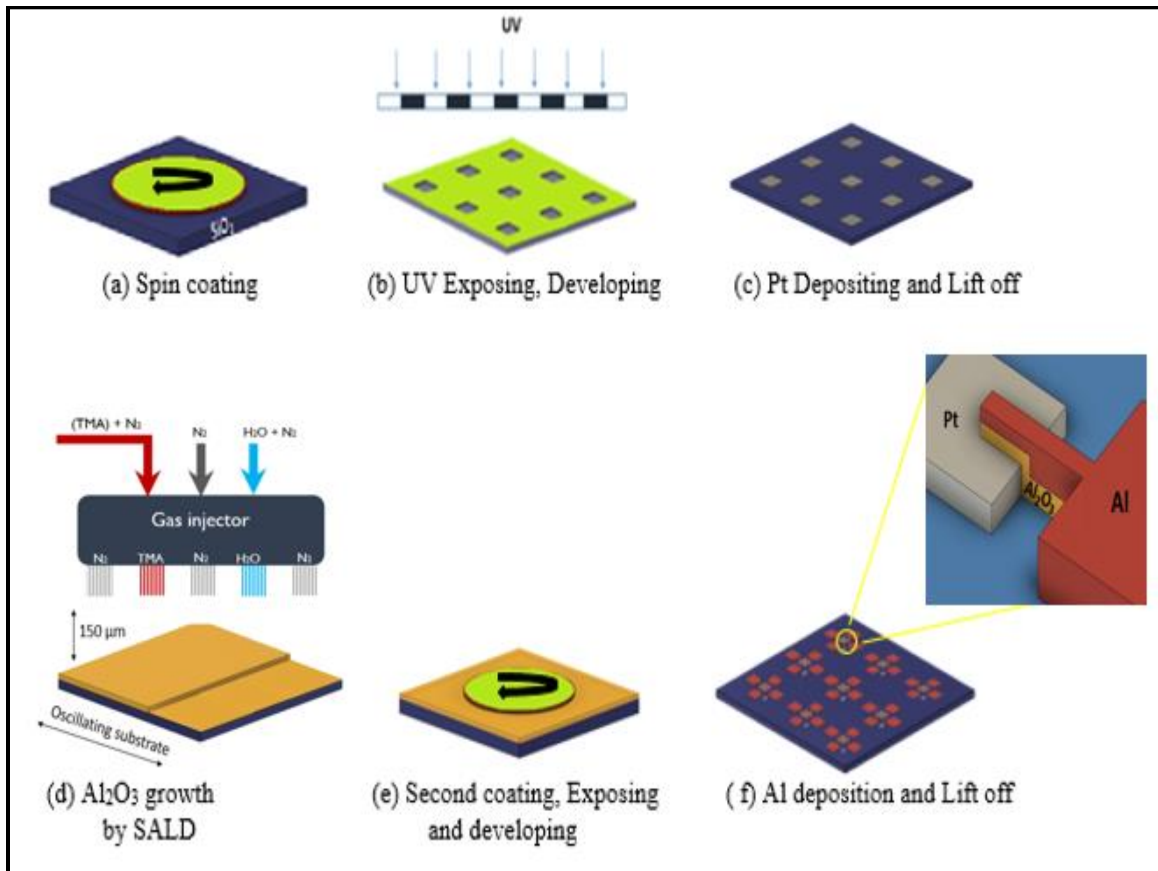

Figure 2.5 Summary of fabrication process of Pt/Al_2O_3/Al diode using AP-SALD.

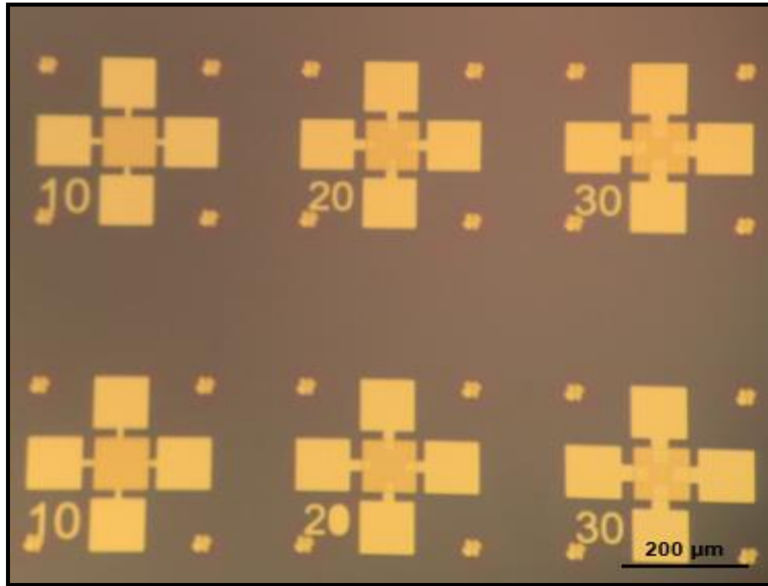

Figure 2.6 Fabricated MIM diodes. The diode with smallest contact area (labelled 10, which means 10 µm x 10 µm) is measured in this work.

2.2 Results and Discussion

A Keithley 4200-SCS semiconductor characterization system connected to a probe station has been applied to measure the DC properties of the MIM diodes, as shown in Figure 2.7.

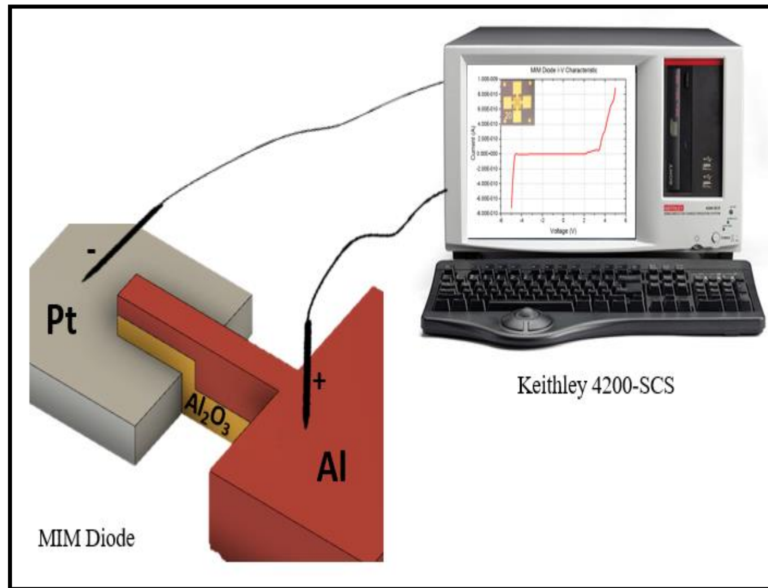

Figure 2.7 Schematic diagram of MIM diode characterization system.

The I-V curves of the MIM diodes were measured using the Keithley system, then the FOMs of the diodes (asymmetry, nonlinearity and responsivity) were calculated from the I-V curves. Pt-Al_2O_3-Al diodes have been fabricated to investigate a novel technique (AP-SALD) for MIM diode fabrication. I-V measurement was applied on many diodes for a voltage range -2V to +2V and the average I-V curves for those diodes is determined, as show in Figure 2.8a. An asymmetrical and nonlinear I-V curve is observed in Figure 2.8.a for a voltage range of -2 V to +2V. A small current (0.15nA) is measured for this diode due to the reasonably thick Al_2O_3 layer (8nm). The work function difference between the Pt and Al metals results in asymmetric tunneling and an asymmetry that reaches 10 at +/-2 V, as shown in Figure 2.8.b. Nonlinearity and responsivity are calculated at the turn-on region. The maximum nonlinearity and responsivity were 26 and 2A/W respectively at the turn-on voltage (+1.1V), as shown in Figure 2.8c, d. These results demonstrate that AP-SALD is suitable for depositing insulator films for MIM diodes. Table 3 shows Figures of Merit for some previously-reported Pt-Al_2O_3-Al diodes. The asymmetry and nonlinearity reported here are higher than in previous studies[40-42]. The greater thickness of the

fabricated diodes in this work causes low responsivity compared to some of the previously-reported work, The responsivity shows low values at low forward currents. Thus, Alumina with smaller thicknesses (<8nm) is required to improve the FOM of the diodes and this is demonstrated in chapter 3 by using a novel combinatorial high throughput AP-SALD technique.

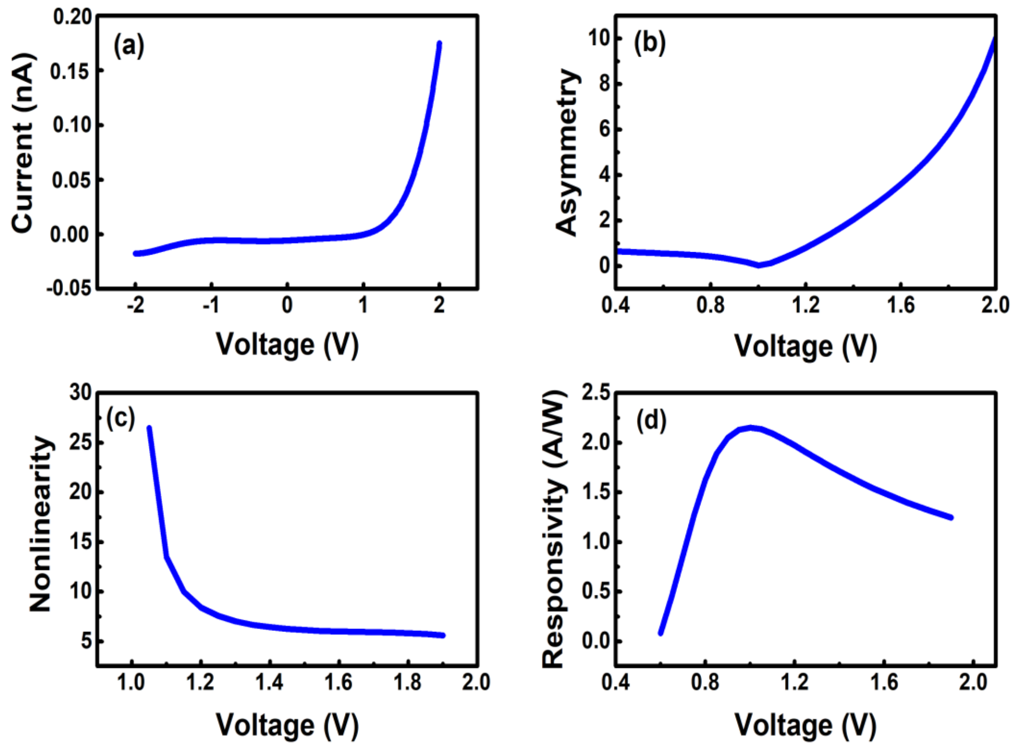

Figure 2.8 I-V characteristics of the Pl-Al_2O_3-Al diodes. (a) I-V curve. (b) Asymmetry with voltage. (c) Nonlinearity with voltage. (d) Responsivity with voltage.

Table 3. Previous reported works for Al-Al_2O_3-Pt diode. (Al-Al_2O_3-Pt: means Al deposited as first contact and the Pt is the second)

Diode Structure	Al_2O_3 thickness (nm)	Maximum Asymmetry	Maximum Nonlinearity	Maximum Responsivity (A/W)
Al-Al_2O_3-Pt (0.008 μm^2)[40]	1	1	$9.9x10^{-6}$ (Linear curve)	$1.24x10^{-3}$
Al-Al_2O_3-Pt (0.004 μm^2)[41]	1 - 2.5	2	Not calculated (Linear curve)	4.8
Al-AlOx-Pt (0.004 μm^2)[42]	2-3.5	1	Not calculated (Linear curve)	5
This Work **Pt-Al_2O_3-Al (100μm^2)**	8	10	26	2.2

.

Chapter 3
Combinatorial MIM Diodes Studies

3.1 Experimental

Pt-Al_2O_3-Al diodes were fabricated by the same process presented in Chapter 2. AP-SALD was implemented to deposit the Al_2O_3 film with a thickness gradient as opposed to a film with uniform thickness. This combinatorial study investigates the influence of thickness of the insulator layer on MIM diodes, and allows several thicknesses to be studied at once. A thickness range of 2.4±0.2 to 8.5 ±1.9 nm was obtained by placing the deposition head on an incline, where the separation between the head and the substrate was 100 µm on one side and 150 µm on the other side, as shown in Figure 3.1. The head-substrate separations used here are sufficiently large that some mixing of the precursors occurs in the gas-phase, resulting in some chemical vapour deposition (CVD). By varying the head-substrate separation across the substrate, the amount of CVD was varied, resulting in different deposition rates across the substrate. It is noted that although CVD is occurring rather than true ALD, it has been shown that smooth, pinhole-free films are still produced, with thicknesses proportional to the number of cycles[43]. Dilute sodium hydroxide (NaOH) was used to etch a small portion of Al_2O_3 on the substrate before depositing the second metal (Al), in order to measure the thickness gradient of the Al_2O_3 film by Atomic Force Microscopy (AFM). Figure 3.2 illustrates the high throughput Pt-Al_2O_3-Al diodes formed on a single substrate, where each row has 18 diodes with different Al_2O_3 thicknesses.

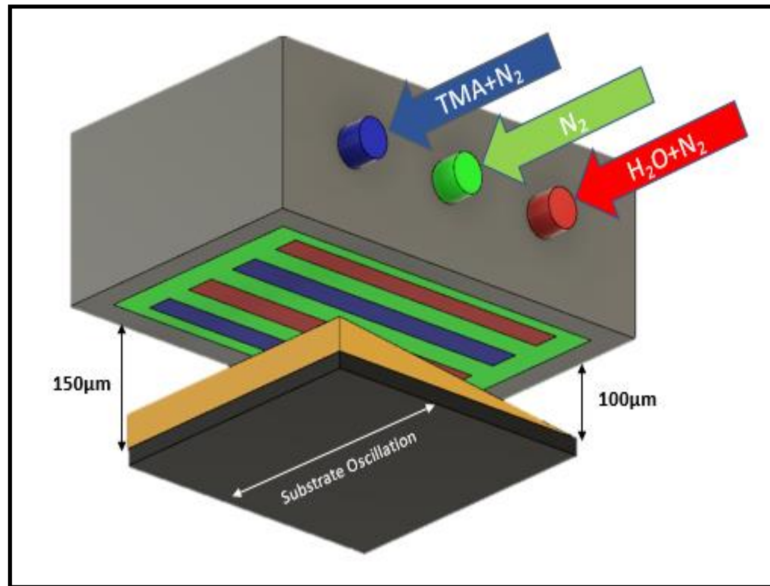

Figure 3.1 A schematic illustration of thickness gradient Al_2O_3 film deposition by AP-SALD.

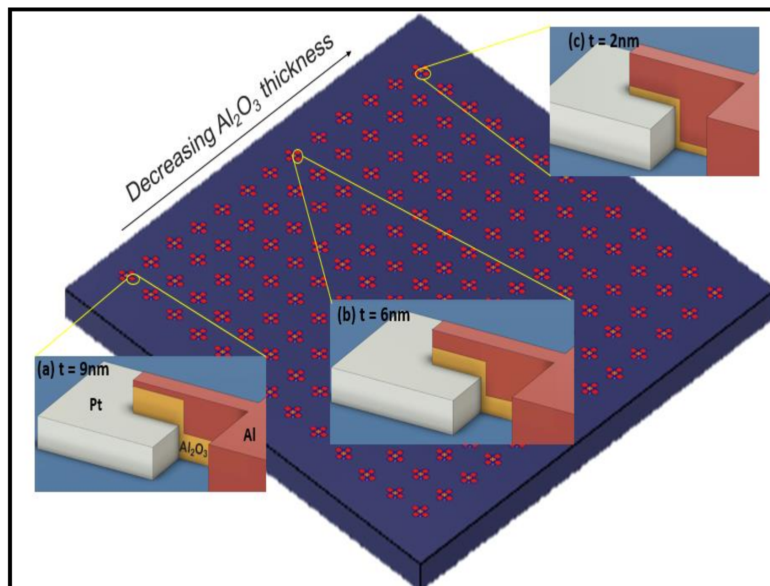

Figure 3.2 Thickness gradient MIM diode architecture.

3.2 Results and Discussion

The AFM image in Figure 3.3 demonstrates the relation of etched film distance versus step height. The Al_2O_3 thickness is seen to vary from approximately 10 nm on one side of the substrate, to approximately 2.5 nm on the other side of the substrate, clearly showing the novelty of this CHT technique. AP-SALD shows the ability to produce sub-10nm thickness gradients using a rapid, atmospheric deposition technique. I-V characteristics are measured for the 18 combinatorial diodes and are shown in Figure 3.4. The I-V curves show asymmetrical and nonlinear curves for the thicker diodes with insulator thicknesses of 6 to 8.5 ±1.9 nm, as shown in Figures 3.4a,b. In contrast, the I-V curve shows low asymmetry and nonlinearity for a thinner insulator layer, as shown in Figure 3.4c. The turn-on voltage (TOV) is seen to decrease from ±4 to ±1.5 V as the insulator becomes thinner. Many diodes for each thickness were tested to calculate the average FOMs with standard deviations. Figures 3.4d, e, f study the relation of Al_2O_3 thickness with asymmetry, nonlinearity and responsivity, respectively. The asymmetry is calculated at the maximum voltage for each diode and is seen to increase with Al_2O_3 thickness in Figure 3.4d, reaching a maximum value of 100 at 6.5nm Al_2O_3 thickness at 3V. The asymmetry decreases for insulator thicknesses larger than 6.5nm. This is attributed to an increase in reverse current with increasing voltage, which decreases the asymmetry ratio. The nonlinearity and responsivity are calculated at 3V and achieve maximum values of 15 and 7A/W respectively at 7 nm of Al_2O_3. These combinatorial high throughput results indicate that the optimum diode FOMs are found in Pt-Al_2O_3-Al diodes with an insulator thickness of 6.5 to 7nm.

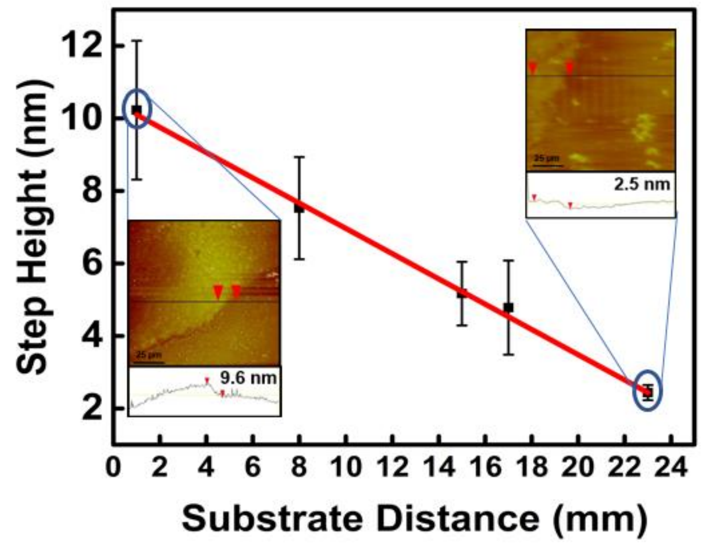

Figure 3.3 Measurement of thickness gradient across an Al_2O_3 film using AFM.

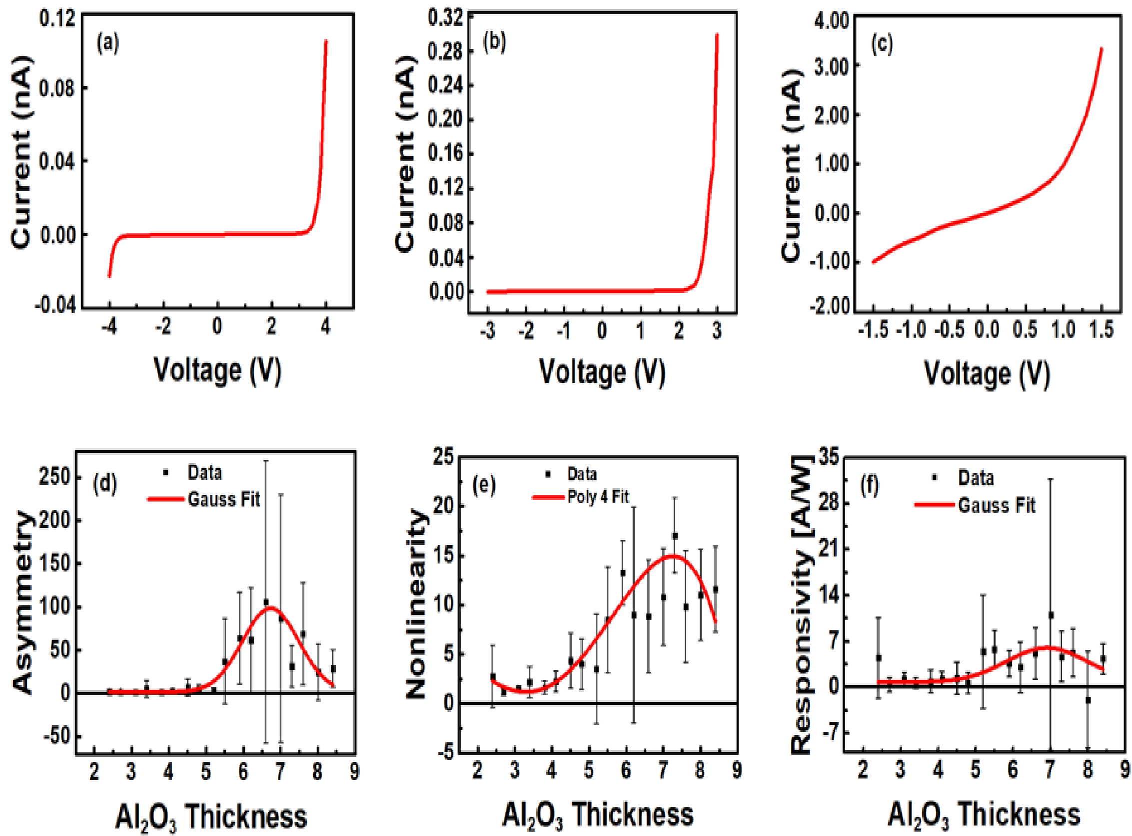

Figure 3.4 I-V curves of different Al_2O_3 thickness for $Pt/Al_2O_3/Al$ diodes: (a) 8.5 ±1.9 nm (b) 6 ±1.9 nm (c) 2.4 ±0.2 nm. Figures of merit for 18 different Al_2O_3 diode thicknesses are calculated and plotted in (d), (e), (f) as asymmetry, nonlinearity, and responsivity respectively.

Chapter 4

Nitrogen Doping Titanium Dioxide (N Doping TiO_2) by PAALD

4.1 Objective

The insulator layer of a MIM diode has a significant role in its rectification performance. Periasamy et al. [9] showed the improvement in the rectification by using various insulator layers. An insulator layer that has an electron affinity close to one of the metal work functions, results in a low potential barrier height. A low potential barrier height can improve rectification performance by minimizing the turn on voltage (TOV), and increasing the current asymmetry and nonlinearity. PAALD is used for N doping of TiO_2 to tune its electron affinity, which is expected to improve the rectification of the diode[44].

A new, simple, economical, and fast approach for PAALD of N-doped TiO_2 with high nitrogen content and substitutional doping was designed and studied. Doping TiO_2 with nitrogen requires high energy because breaking of the Ti-O bonds by nitrogen atoms is not thermodynamically favored[37]. In a previous PAALD study, when the nitrogen plasma flow was increased, only interstitial-N doped TiO_2 was observed, and the N concentration in the TiO_2 was low[45]. In the presented approach, a pure nitrogen plasma was used instead of an oxygen O_2 precursor (unlike the mixed H_2/N_2 plasma used by Zhang et al.[33]), so that the formation of Ti-O bonds is inhibited and nitrogen is more likely to react with the Ti. Residual water vapor in the PAALD chamber was an oxygen source at a pressure range of 10^{-6} to 10^{-7} torr, thus titanium isopropoxide was selected as the titanium precursor because it is highly reactive with water vapor. Even though there is very little water vapor in the chamber as compared to nitrogen, its affinity for the Ti precursor is much greater, which is expected to ensure the formation of N-doped TiO_2 in this arrangement, rather than TiN. However, by limiting the quantity of oxygen present and using a pure N_2 plasma, it is expected that nitrogen incorporation into the films will be enhanced and result in more substitutional doping of TiO_2.

4.2 PAALD of N-Doped TiO_2

Nitrogen-doped TiO_2 was deposited on glass substrates that were 25.4±0.2 mm in diameter and 1.6±0.2 mm thick at 250 °C in an Oxford- FlexALTM system with a base pressure below 10^{-6} torr. The system utilized an inductively coupled plasma (ICP) source for remote plasma operation. The diameter of the ICP tube was 80 mm, and the loadlock of the system pumped to below 10^{-5} torr. The vacuum chamber was first purged with Ar for 3 min to stabilize the chamber pressure and temperature. Figure 4.1 illustrates the N-doped TiO_2 recipe used in this work, along with that of Zhang et al.[33]. Titanium isopropoxide (TIIP) bubbled with argon was used to dose the substrate for 2s at a pressure of 80 mT then the precursor line was purged with Ar for 3 s at a pressure of 15 mT. For a few depositions, a flow of O_2 was then stabilized for 500 ms before generating a plasma by radio frequency (RF) with a power of 300 W at a pressure of 15 mT. The substrate was exposed to the O_2 plasma then purged with Ar for 2s at a pressure of 80 mT. The N_2 plasma flow was stabilized for 500 ms and a RF plasma was generated with a power of 300 W. The substrate was exposed at a pressure of 15 mT, followed by purging for 2 s at a pressure of 80 mT.

The O_2 and N_2 gas feeds, plasma exposure times, and number of PAALD cycles for different recipes tested are summarized in Table 4. Notably all recipes except the TiO_2 recipe and the first doping recipe did not employ the oxygen plasma, such that the only sources of oxygen were the TIIP and residual water vapor in the vacuum chamber.

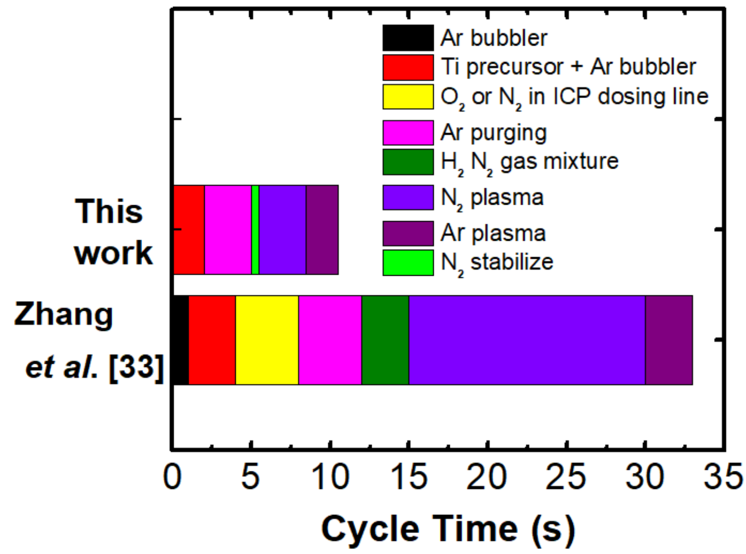

Figure 4.1. Flow chart of PAALD cycle developed in this work and cycle reported in previous work[33]. Recipes that produced the highest nitrogen contents are shown.

Table 4: Process recipes for PAALD films.

Procedure	Gas feed (sccm)		Plasma time (s)	No.of cycles	Base pressure
	O_2	N_2			
1	10	50	3	300	$5x10^{-6}$ Torr
2	0	50	1	300	
3	0	50	3	300	
4	0	50	5	300	
5	0	50	7	300	
TiO_2	60	0	3	300	

4.2.1 Characterization of N -Doped TiO_2

The samples were characterized by UV-Vis spectroscopy (UV-2501 PC) with a 190-1100 nm wavelength range, resolution of 0.1 nm, wavelength accuracy of ± 0.3 nm, and precision of ±0.002 abs. The UV-vis measurements were applied to identify the band gap of the N-doped TiO_2. The absorption coefficient α was calculated using the formula $\alpha = 2.303\ (A/t)$ where A is the absorbance, t is the film thickness and 2.303 is calculated from a conversion factor ln (10) [46]. The band gaps of the films were calculated from Tauc plots[47] by plotting $(\alpha h\nu)^{1/2}$ versus the photon energy $h\nu$, where the tangent of the curve gives the band gap of the film. X-ray photo electron spectroscopy (XPS) (VG Scientific ESCALAB 250), was performed on the surface of the films using Al Kα x-rays. The spectra were calibrated using the C1s peak at 284.6 eV. A Woollam M-2000 DI ellipsometer was used to measure the thickness of N-doped TiO_2 films deposited on Si wafers (100 orientation) that were 2 inches in diameter and 330.2 to 431.8 microns thick.

4.3 Result and Discussion

UV-vis transmission measurements of the N-doped TiO_2 films in Figure 4.2a show a shift in the absorbance edge from 350 nm for TiO_2 to 370 nm for the first recipe (3s O_2 and N_2 plasmas), 460 nm for the second recipe (1s N_2 plasma), 520 nm for the third recipe (3s N_2 plasma), and 500 nm for the fourth and fifth recipes (5s and 7s N_2 plasma respectively), indicating the successful incorporation of nitrogen in all cases. The optical band gap of the deposited films was determined using Tauc plots[47], as shown in Figure 4.2b. The narrowing of the band gap from 3.1eV for TiO_2 to 1.8 eV for the films deposited using the third recipe (3s N_2 plasma) is consistent with previous reports[37] that showed narrowing in band gap to 1.91 eV. The thicknesses of the samples were measured by ellipsometry to be 11.5±0.3 nm (3s O_2 and N_2 plasmas), 11.1±0.2 nm, (1s N_2 plasma), 10.5±0.1 nm (3s N_2 plasma), 10.2±0.4 nm (5s N_2 plasma), 8.7±0.1 nm (7s N_2 plasma) and 14.4±0.2 nm for TiO_2..

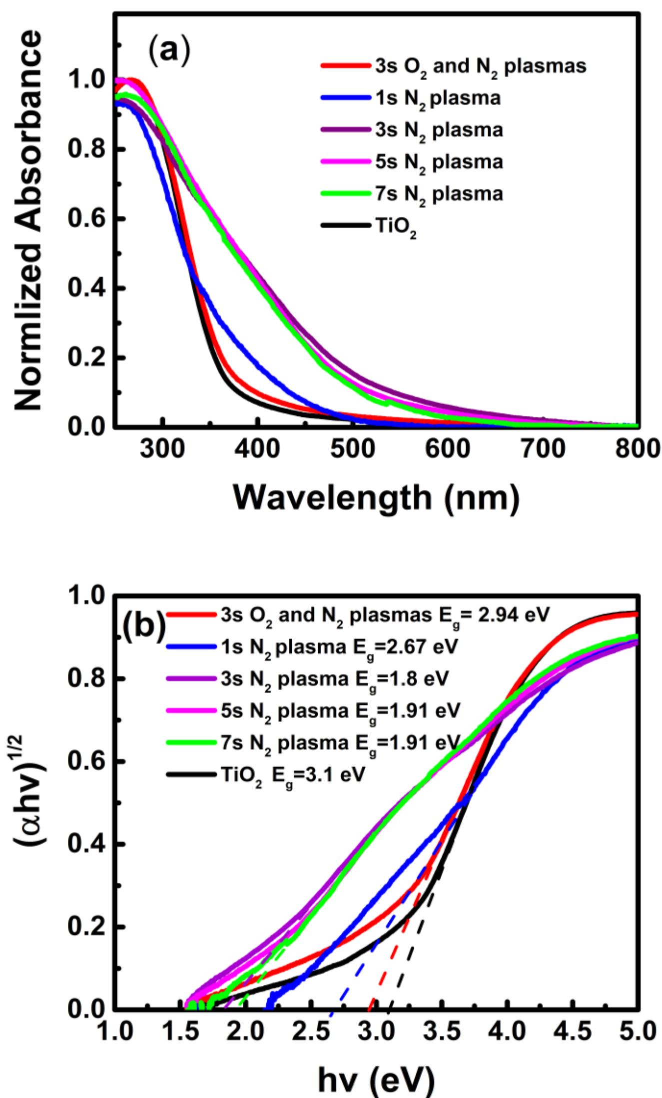

Figure 4.2 (a) UV-vis spectra of TiO_2 and N- doped TiO_2 films (b) Tauc plotting of UV-vis spectra of TiO_2 and N-doped TiO_2 films.

The chemical composition and bonds between elements were characterized by XPS, as shown in Figure 4.3. The moderate deposition temperature of 250 °C was selected to prevent the formation of TiN rather than TiO_2. Table 5 compares the XPS peak positions observed in this work with those of TiN, TiNO, and

N-doped TiO_2 reported previously in literature. It is seen that the Ti $2p_{3/2}$ and Ti $2p_{1/2}$ peaks observed are consistent with previous reports of N-doped TiO_2. Ti $2p_{3/2}$ and Ti $2p_{1/2}$ peaks are located at 458 eV and 464 eV respectively for the TiO_2 recipe in Figure 4.3a, and are attributed to TiO_2 (Ti^{4+}). For the first recipe (3s O_2 and N_2 plasmas), two more peaks with small intensities are observed in Figure 4.3b at 457 eV and 463 eV, which are attributed to Ti_2O_3 (Ti^{3+}). Using nitrogen plasma without O_2 gas in recipes 3-5 resulted in an increase in the Ti^{3+} peak intensities, as shown in Figures 4.3d-f, demonstrating that the Ti^{3+} peaks appear when the nitrogen content is increased in the films[48]. Figure 4.4 shows the relative Ti^{4+} and Ti^{3+} peak intensities as a function of increasing nitrogen plasma exposure. The Ti^{4+} peak contribution is high when O_2 plasma is present in the chamber, as shown in the TiO_2 and first (3s O_2/N_2) recipes. Eliminating the O_2 gas source in the chamber resulted in an increase in the fraction of Ti^{3+} in the film, as shown in the second (1s N_2 plasma) and third (3s N_2 plasma) recipes. Interestingly the Ti^{3+}/Ti^{4+} ratio decreased for the longer 5s and 7s N_2 plasma exposures (recipes 4 and 5). This trend suggests that approximately 3s is required for the N_2 plasma to react with the Ti precursor, but that for longer plasma exposure times, the small amount of residual water vapor in the chamber may react with the Ti precursor, replacing the nitrogen with oxygen.

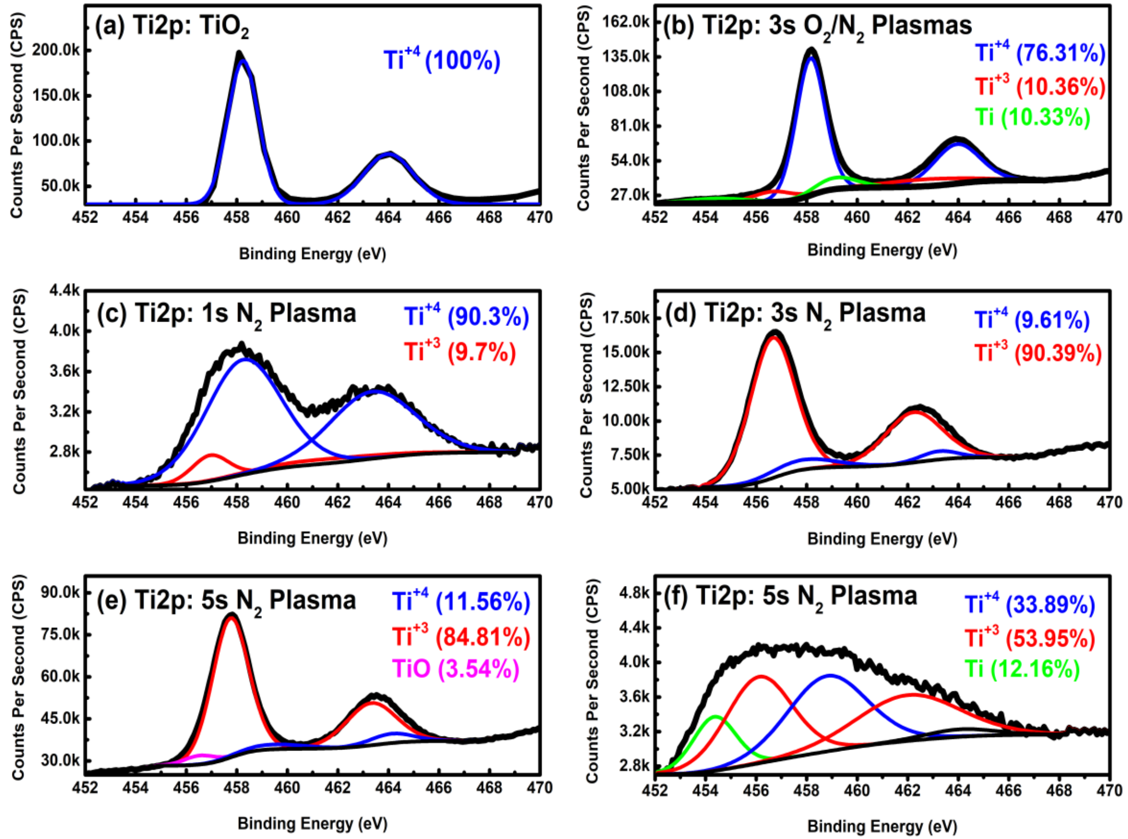

Figure 4.3: Ti 2p XPS spectra of TiO_2 and N-doped TiO_2 films: (a) TiO_2 (b) 3s O_2/N_2 plasmas (c) 1s N_2 plasma (d) 3s N_2 plasma (e) 5s N_2 plasma (f) 7s N_2 plasma.

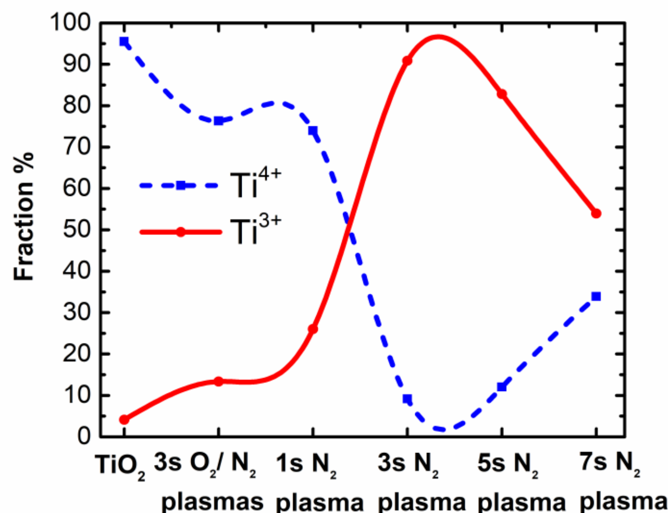

Figure 4.4: Ti^{4+} and Ti^{3+} peak intensities for increasing nitrogen plasma exposure.

Figure 4.5 shows that N1s XPS peaks are present for all recipes that employed the N_2 plasma, confirming that nitrogen is incorporated successfully into the TiO_2 lattice. N1s XPS peaks from 396 to 398 eV and 399 to 401 eV have previously been assigned to substitutional and interstitial nitrogen respectively[49]. Figures 4.5a shows a weak N peak (Ti-O-N) at 400 eV for the TiO_2 recipe, which is attributed to chemisorbed N_2 [32, 50]. Recipe 1, which employed 3s O_2 and N_2 plasmas, shows a dominant peak (Ti-O-N) at approximately 400 eV in Figure 4.5b, which has previously been reported to correspond to interstitial doping[51]. Recipe 2 (1s N_2 plasma) shows only a weak interstitial nitrogen peak (Ti-O-N) located at approximately 400 eV in Figure 4.5c, indicating that the 1s N_2 plasma was insufficient to incorporate a significant amount of nitrogen. Substitutional nitrogen peaks, which are located at approximately 396 eV and 398 eV, are assigned to O-Ti-N[52] and N-Ti-O[53] respectively. The relative intensities of these two substitutional peaks has been reported to be different for different fabrication processes. Iri *et al.*[52] showed that nitrogen substitutes for oxygen and forms a O-Ti-N bond with a N1s peak at approximately 396 eV when the samples were annealed at 550 °C under O_2, N_2, or NH_3 gas flow.

Sathish *et al.*[53] showed a substitutional peak at 398 eV, assigned to N-Ti-O bonding, indicating that a N^- anion combines with TiO_2. When the amount of nitrogen substituted in TiO_2 sites is small, the 396 eV peak appears[49]. This peak is observed in this work for films made using recipes 1, 3, and 4 (Figures 4.5b, 4.5d, and 4.5e), where it corresponds to small proportions of the total N1s signal (5.3%, 6.4%, and 13.9% respectively). The substitutional peak at 398 eV, which is attributed to the N^- anion, is expected to be responsible for changing the Ti^{4+} valence state[49]. This agrees with measurements in this work, as it is seen in Figure 4.5d that the peak at 398 eV (N-Ti-O N1s) is a maximum (93%) for recipe 3 (3s N_2 plasma), whereas the intensity of the Ti 2p XPS signal attributed to Ti^{4+} drops dramatically for the film produced by recipe 3, as summarized in Figure 4, and the signal corresponding to Ti^{3+} reaches a maximum value (~95%). The substitutional nitrogen peaks are highest for the 3s N_2 plasma exposure (Recipe 3) in Figure 4.5d, then decrease for longer exposure times (Recipes 4 and 5), as seen in Figures 4.5e-f. These results suggest that approximately 3s is required for the N_2 plasma to react with the monolayer of Ti precursor, and that for longer N_2 plasma exposure times, Ti-N bonds are broken by subsequent thermodynamically-favored titanium-oxygen reactions, consistent with the observed decrease in Ti^{3+}/Ti^{4+} ratio in Figure 4.4. In particular, the increase in the interstitial Ti-O-N peak with plasma exposure time observed in Figures 4.5d-f suggests that reactions between the titanium precursor and residual water in the chamber result in nitrogen atoms being moved from substitutional to interstitial positions, as oxygen atoms take their place.

The location of nitrogen atoms in the TiO_2 lattice is important for catalyst performance[54]. By varying the N_2 plasma exposure time, control over the position of nitrogen in TiO_2 was successfully demonstrated using this PAALD method. Table 6 summarizes the fraction of interstitial and substitutional doping achieved with the various recipes, as determined by comparing the area under the interstitial and substitutional XPS peaks in Figure 4.5 to the total area under the N1s peak. It is seen that with Recipe 3 (3s N_2 plasma), over 99% substitutional doping can be achieved, higher than that reported previously for

PAALD[33]. Furthermore, the fraction of interstitial doping can be increased by increasing the N_2 plasma exposure time or introducing an O_2 plasma.

Table 6 also summarizes the film compositions calculated from the XPS spectra. A Si contribution is observed from the glass substrate for some samples where a larger measurement voltage was required. The observed carbon contamination is consistent with previous reports that used TIIP and oxygen plasma[35]. The high carbon contaminations observed (e.g. for recipes 3 and 4) may be due to incomplete reaction between the TIIP and the nitrogen plasma, which could leave significant amounts of unreacted precursors. Zhang *et al.*[33] also observed a significant amount of carbon with the incomplete reaction of tetrakis (dimethylamino) titanium (TDMAT) with nitrogen. Air contamination resulting from transporting the samples to the XPS equipment is also expected. A sample prepared using recipe 3 (3s N_2 plasma) was annealed at 400°C for 1 hour in air and XPS measurement were repeated. The carbon content decreased from over 42±0.5 at.% to 28.3±0.1 at.%, consistent with the removal of contaminants or unreacted precursors. Annealing of the as-deposited samples, however, was also observed to result in the formation of thermodynamically favored Ti-O bonds, as evidenced by an increase in the oxygen content to 49.7±0.3 at.%, significant reduction in the nitrogen content to 3.2±0.4 at.%, and shift of the nitrogen signal from substitutional peaks to interstitial peaks, consistent with the findings of Deng *et al.*[37]

The nitrogen concentration of 27.2±0.5 at.% that is observed for the film deposited with 3s N_2 plasma exposures (Recipe 3) is higher than that reported for previous PAALD of N-doped TiO_2,[33, 36, 37] and uses a N_2 plasma exposure time that is 5 times shorter than that used by Zhang et al.[33] to produce a nitrogen content of %13 at the film surface (%22 in the bulk). The resulting cycle time (10.5 s/ cycle) is 3 times shorter than that used by Zhang et al.[33], as shown in Figure 4.1. However, given the large carbon and oxygen contamination observed in this work, as discussed above, caution must be taken when comparing the observed nitrogen content to previous work. As noted in Figure 5a, even the TiO_2 procedure revealed a weak N1s XPS peak due to nitrogen contamination. Nonetheless, this recipe

demonstrates the ability of a N_2 plasma environment to dope TiO_2 more effectively than some plasma environments that make use of NH_3[55]. The nitrogen content is observed to decrease from 27.2±0.5 to 21.6±0.4 and 1±0.5 at.% for longer N_2 plasma exposure times of 5s and 7s (Recipes 4 and 5). This suggests that the thermodynamically favored reactions between the titanium isopropoxide and residual water vapor that occur at longer timescales not only result in a shifting of nitrogen dopants from substitutional to interstitial positions, as detailed in Figure 4.5, but also result in the gradual expulsion of the nitrogen atoms from the films. Figure 4.6 shows the O1s peaks for the samples. The very high affinity of titanium for oxygen[56] is expected to result in the Ti precursor atoms accommodating all available oxygen in the chamber. By using a recipe with no O_2 plasma (Recipe 3), the Ti-O bond intensity is decreased, as shown in Figure 4.6b. It is expected that limiting the formation of Ti-O bonds enables the incorporation of more nitrogen atoms into the films (substitutional and interstitial) when they are exposed to the nitrogen plasma.

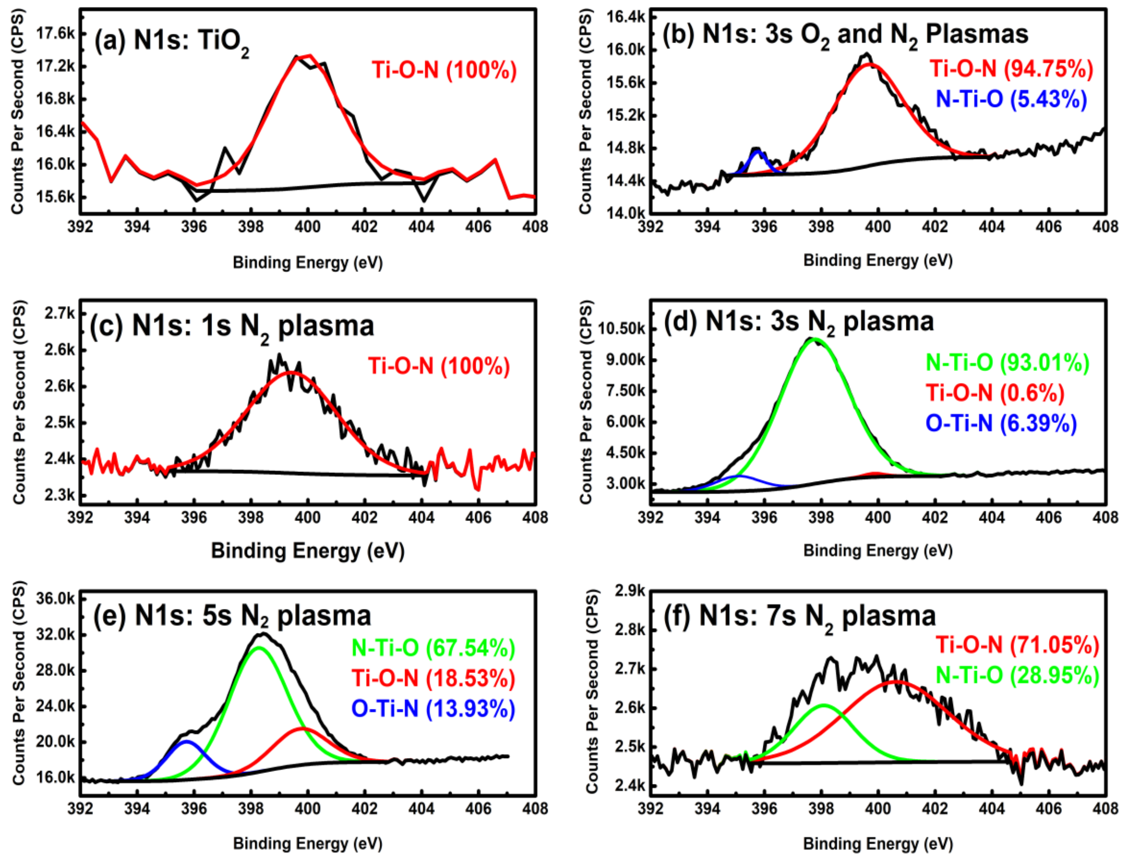

Figure 4.5: N1s XPS spectra of TiO_2 and N-doped TiO_2 films: (a) TiO_2 (b) 3s O_2/N_2 plasmas (c) 1s N plasma (d) 3s N plasma (e) 5s N plasma (f) 7s N plasma.

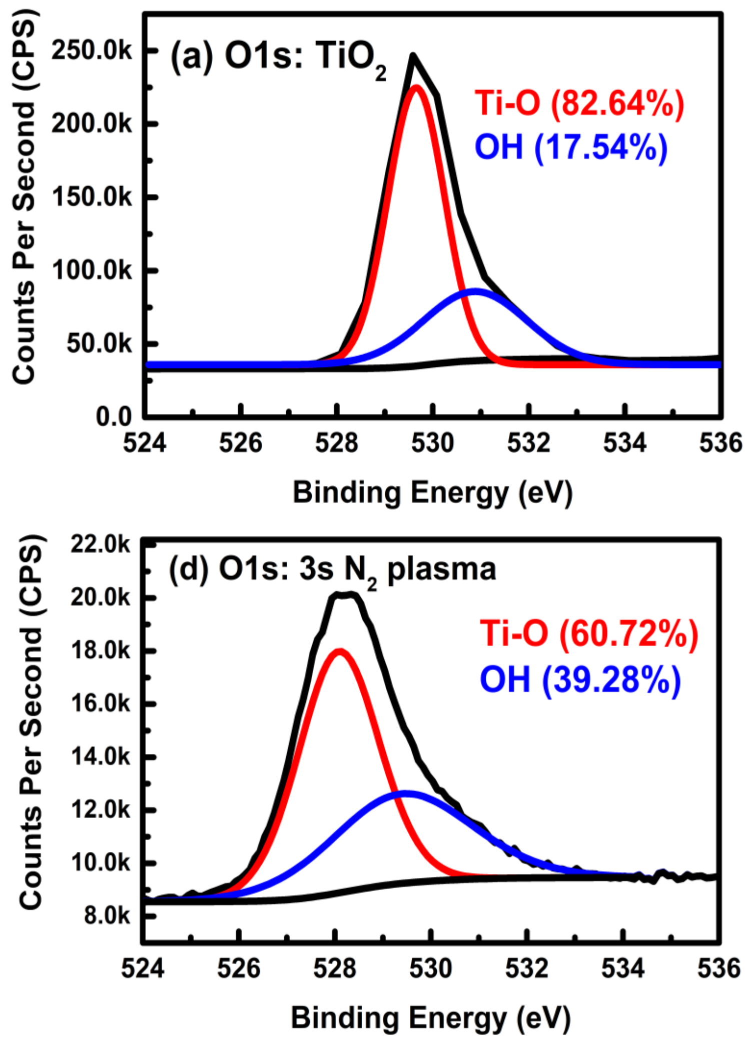

Figure 4.6. O1s XPS spectra of TiO_2 and N-doped TiO_2 films: (a) TiO_2 (b) 3s N.

Table 5: Literature Data on the XPS binding energies (eV) of Ti 2p, N 1s, and O 1s [65].

Films	Ti $2p^{3/2}$	Ti $2p^{1/2}$	N 1s	O 1s
TiN	455.2[57] 455.9[58]	461[37]	396[59] 397[60]	Ti-O 531[57]
TiNO	455.2 [61]	461[61]	397[60]	Ti-O 531[57]
N-Doped TiO_2	456-459[59] 459.1[60]	464.4[62] 463-465[59]	Ti-O-N 400[51] N-Ti-O 398[63] O-Ti-N 396[64]	Ti-O 529.7[57] titanium suboxides 531[37]
This work	Recipe 1: 458.5	464	400 (Ti-O-N) interstitial	Ti-O 529.7 OH 531±0.2
	Recipe 2: 458.5	464	400 (Ti-O-N) interstitial	Ti-O 529.7 SiO_2 (534)
	Recipe 3: 457	463	398 (substitutional)	Ti-O 528.7 OH 530
	Recipe 4: 457.4	462.5	400,398,395.4 (subs. + interst.)	Ti-O 529.7 OH 531±0.2
	Recipe 5: 457	463	400,396 (subs. + interst.)	Ti-O 529.6 SiO_2 534
	TiO_2 : 458.5	464	-	Ti-O 529.6 titanium suboxides 531.1

Table 6: Film compositions of PAALD samples.

Procedure	Film Compositions (at%)						Fraction (%)[a]	
	Ti	O	N	C	Si	N/Ti	N_{inte}	N_{sub}
1	22.5±0.6	52.1±0.3	1.6±0.1	23.7±0.1	-	0.1	94.7	5.4
2	1.3±0.8	45.4±6	0.4±0.3	16.5±0.4	36.1±0.4	0.3	100	0
3	9.7±1	20.9±0.6	27.2±0.5	42.1±0.5	-	2.8	0.6	99.4
4	13.9±0.7	30.1±0.5	21.6±0.4	34.2±0.3	-	1.6	18.5	81.4
5	2.3±0.9	45.6±1	1±0.5	16.9±0.7	34±0.5	0.4	29	71
TiO_2	23.4±0.4	40.9±0.3	0.7±0.2	21.1±0.3	13.7±0.1	0.03	-	-

a: Calculated based on the area of the Ninterstitial and Nsubstitutional peaks, compared to the total area of the N1s peaks.

Chapter 5
Conclusion and Future work

Novel MIM diodes were fabricated by atmospheric pressure spatial atomic layer deposition (AP-SALD). This scalable method was used to produce MIM diodes with high-quality, pinhole-free insulator films more rapidly than by conventical ALD.

Combinatorial and high-throughput (CHT) MIM diodes were fabricated and characterized. Pt-Al_2O_3-Al diodes with an insulator thickness gradient were introduced. The diode FOMs showed variation with Al_2O_3 thickness and the best diode performance was found at 6.5 to 7nm thickness, where the asymmetry, nonlinearity and responsivity were 100, 15, and 7A/W respectively.

A simple and fast PAALD technique to dope TiO_2 with nitrogen was demonstrated. UV-visible measurements showed narrowing of the band gap from 3.1 to 1.8 eV. XPS characterization demonstrated higher nitrogen content (27.2±0.5 at%) than reported previously for nitrogen doping with PAALD. This effective method required no O_2 precursor, high temperatures, or post chemical treatments to enhance the N content in the TiO_2 films. It required only one reactant plasma with a short exposure time (1 to 7s). Furthermore, it was demonstrated that the fraction of interstitial and substitutional doping could be tailored by varying the plasma exposure time, with >99% substitutional or interstitial doping possible.

As future work, frequency-dependent characterization of the diodes and altering of the diode geometry to enable high-frequency operation and characterization should be investigated. In addition, MIM diodes with different material combinations that are expected to produce better Figures of Merit than Pt-Al_2O_3-Al should be studied. This includes diodes incorporating N-doped TiO_2, and diodes with multiple insulator layers with thicknesses optimized using combinatorial AP-SALD.

-

Bibliography

1. W. Brown, J. Mims, N. Heenan: in 1958 IRE Int. Convention Rec, 225-235 (1966)

2. V. Mlinar: Nanotechnology 4, 042001 (2013)

3. E. Donchev, J.S. Pang, P.M. Gammon, A. Centeno, F. Xie, P.K. Petrov, J.D. Breeze, M.P. Ryan, D.J. Riley, N.M. Alford: MRS Energy & Sustainability, E1 (2014)

4. H. Pagnia: International journal of electronics 5, 695-705 (1994)

5. H. Liu, B. Chen, X. Li, W. Liu, Y. Ding, B. Lu: Nanotechnology 45, 455302 (2011)

6. I.D. Parker: J. Appl. Phys. 3, 1656-1666 (1994)

7. P. Periasamy, H.L. Guthrey, A.I. Abdulagatov, P.F. Ndione, J.J. Berry, D.S. Ginley, S.M. George, P.A. Parilla, R.P. O'Hayre: Adv Mater 9, 1301-1308 (2013)

8. N. Alimardani, J.F. Conley Jr: Appl. Phys. Lett. 8, 082902 (2014)

9. A. Sanchez, C. Davis Jr, K. Liu, A. Javan: J. Appl. Phys. 10, 5270-5277 (1978)

10. M. Abdel-Rahman, M. Syaryadhi, N. Debbar: Electron. Lett. 5, 363-364 (2013)

11. E.G. Ozkan, M. Inac, A. Shafique, M. Ozcan, Y. Gurbuz: , 98190F-98190F-5 (2016)

12. P. Periasamy, J.J. Berry, A.A. Dameron, J.D. Bergeson, D.S. Ginley, R.P. O'Hayre, P.A. Parilla: Adv Mater 27, 3080-3085 (2011)

13. S. Sharma, M. Khawaja, M.K. Ram, D.Y. Goswami, E. Stefanakos: Beilstein journal of nanotechnology 1, 2240-2247 (2014)

14. N. Alimardani, J.M. McGlone, J.F. Wager, J.F. Conley Jr: Journal of Vacuum Science & Technology A: Vacuum, Surfaces, and Films 1, 01A122 (2014)

15. K.P. Musselman, C.F. Uzoma, M.S. Miller: Chemistry of Materials 23, 8443-8452 (2016)

16. R. Potyrailo, K. Rajan, K. Stoewe, I. Takeuchi, B. Chisholm, H. Lam: ACS combinatorial science 6, 579-633 (2011)

17. M. Otani, E.L. Thomas, W. Wong-Ng, P.K. Schenck, K. Chang, N.D. Lowhorn, M.L. Green, H. Ohguchi: Japanese Journal of Applied Physics 5S2, 05EB02 (2009)

18. K. Kennedy, T. Stefansky, G. Davy, V.F. Zackay, E.R. Parker: J. Appl. Phys. 12, 3808-3810 (1965)

19. M. Aronova, K. Chang, I. Takeuchi, H. Jabs, D. Westerheim, A. Gonzalez-Martin, J. Kim, B. Lewis: Appl. Phys. Lett. 6, 1255-1257 (2003)

20. L. Zhong, Z. Zhang, S.A. Campbell, W.L. Gladfelter: Journal of Materials Chemistry 21, 3203-3209 (2004)

21. H.M. Yates, P. Evans, D.W. Sheel, J.L. Hodgkinson, P. Sheel, U. Dagkaldiran, A. Gordijn, F. Finger, Z. Remes, M. Vanecek: ECS Transactions 8, 789-796 (2009)

22. A. Kafizas, I.P. Parkin: Journal of Materials Chemistry 11, 2157-2169 (2010)

23. M. Pavan, S. Rühle, A. Ginsburg, D.A. Keller, H. Barad, P.M. Sberna, D. Nunes, R. Martins, A.Y. Anderson, A. Zaban: Solar Energy Mater. Solar Cells, 549-556 (2015)

24. J. Bai, B. Zhou: Chem. Rev. 19, 10131-10176 (2014)

25. A. Decroly, A. Krumpmann, M. Debliquy, D. Lahem: (2016)

26. K. Vasu, M. Sreedhara, J. Ghatak, C. Rao: ACS applied materials & interfaces 12, 7897-7901 (2016)

27. J. Wang, D.N. Tafen, J.P. Lewis, Z. Hong, A. Manivannan, M. Zhi, M. Li, N. Wu: J. Am. Chem. Soc. 34, 12290-12297 (2009)

28. B. Liu, L. Wen, X. Zhao: Solar Energy Mater. Solar Cells 1, 1-10 (2008)

29. Y. Suda, H. Kawasaki, T. Ueda, T. Ohshima: Thin Solid Films, 162-166 (2004)

30. V. Pore, A. Rahtu, M. Leskelä, M. Ritala, T. Sajavaara, J. Keinonen: Chemical Vapor Deposition 3, 143-148 (2004)

31. V. Pore, M. Heikkilä, M. Ritala, M. Leskelä, S. Areva: J. Photochem. Photobiol. A. 1, 68-75 (2006)

32. H. Cheng, W. Lee, C. Hsu, M. Hon, C. Huang: Electrochemical and Solid-State Letters 10, D81-D84 (2008)

33. Y. Zhang, M. Creatore, Q. Ma, A. El Boukili, L. Gao, M.A. Verheijen, E.J. Hensen: Appl. Surf. Sci., 476-486 (2015)

34. Y. Zhang, Q. Ma, L. Gao, E.J. Hensen: Appl. Surf. Sci., 174-180 (2013)

35. J. Musschoot: Advantages and challenges of plasma enhanced atomic layer deposition (2011)

36. R. Zhipeng, W. Jun, L. Chaobo, C. Bo, L. Jian, H. Chengqiang, X. Yang: Plasma Science and Technology 3, 239 (2014)

37. S. Deng, S.W. Verbruggen, S. Lenaerts, J.A. Martens, S. Van den Berghe, K. Devloo-Casier, W. Devulder, J. Dendooven, D. Deduytsche, C. Detavernier: Journal of Vacuum Science & Technology A: Vacuum, Surfaces, and Films 1, 01A123 (2014)

38. A. Goossens, E. Maloney, J. Schoonman: Chemical Vapor Deposition 3, 109-114 (1998)

39. F. Aydinoglu: (2013)

40. E.C. Kinzel, R.L. Brown, J.C. Ginn, B.A. Lail, B.A. Slovick, G.D. Boreman: Microwave Opt Technol Lett 3, 489-493 (2013)

41. J.A. Bean, B. Tiwari, G.H. Bernstein, P. Fay, W. Porod: Journal of Vacuum Science & Technology B: Microelectronics and Nanometer Structures Processing, Measurement, and Phenomena 1, 11-14 (2009)

42. B. Tiwari, J.A. Bean, G. Szakmány, G.H. Bernstein, P. Fay, W. Porod: Journal of Vacuum Science & Technology B: Microelectronics and Nanometer Structures Processing, Measurement, and Phenomena 5, 2153-2160 (2009)

43. K.P. Musselman, D. Muñoz-Rojas, R.L. Hoye, H. Sun, S. Sahonta, E. Croft, M. Böhm, C. Ducati, J. MacManus-Driscoll: Nanoscale Horizons (2017)

44. K. Mistry, M. Yavuz, K.P. Musselman: J. Appl. Phys. 18, 184504 (2017)

45. H. Profijt, S. Potts, M. Van de Sanden, W. Kessels: Journal of Vacuum Science & Technology A: Vacuum, Surfaces, and Films 5, 050801 (2011)

46. B. Sahu, K.S. Shin, J.G. Han: Plasma Sources Sci. Technol. 1, 015017 (2016)

47. J. Tauc, R. Grigorovici, A. Vancu: physica status solidi (b) 2, 627-637 (1966)

48. K.K. Akurati: Synthesis of TiO_1tn2 Based Nanoparticles for Photocatalytic Applications (Cuvillier Verlag - 2008)

49. B. Viswanathan, K. Krishanmurthy: International Journal of Photoenergy (2012)

50. R. Asahi, T. Morikawa, T. Ohwaki, K. Aoki, Y. Taga: Science 5528, 269-271 (2001)

51. F. Dong, W. Zhao, Z. Wu, S. Guo: J. Hazard. Mater. 2, 763-770 (2009)

52. H. Irie, S. Washizuka, N. Yoshino, K. Hashimoto: Chemical Communications 11, 1298-1299 (2003)

53. M. Sathish, B. Viswanathan, R. Viswanath, C.S. Gopinath: Chemistry of materials 25, 6349-6353 (2005)

54. S.A. Ansari, M.M. Khan, M.O. Ansari, M.H. Cho: New Journal of Chemistry 4, 3000-3009 (2016)

55. D.J. Pulsipher, I.T. Martin, E.R. Fisher: ACS applied materials & interfaces 6, 1743-1753 (2010)

56. M.J. Donachie: Titanium: a technical guide (ASM international - 2000)

57. N.C. Saha, H.G. Tompkins: J. Appl. Phys. 7, 3072-3079 (1992)

58. C.D. Wagner, G. Muilenberg: Handbook of X-ray photoelectron spectroscopy (Perkin-Elmer - 1979)

59. L. Miao, S. Tanemura, H. Watanabe, Y. Mori, K. Kaneko, S. Toh: J. Cryst. Growth 1, 118-124 (2004)

60. G. Battiston, R. Gerbasi, A. Gregori, M. Porchia, S. Cattarin, G. Rizzi: Thin Solid Films 1, 126-131 (2000)

61. J. Guillot, A. Jouaiti, L. Imhoff, B. Domenichini, O. Heintz, S. Zerkout, A. Mosser, S. Bourgeois: Surf. Interface Anal. 7, 577-582 (2002)

62. M. Maeda, T. Watanabe: J. Electrochem. Soc. 3, C186-C189 (2006)

63. S. Sato, R. Nakamura, S. Abe: Applied Catalysis A: General 1, 131-137 (2005)

64. X. Chen, C. Burda: The Journal of Physical Chemistry B 40, 15446-15449 (2004)

65. C. Chen, H. Bai, C. Chang: The Journal of Physical Chemistry C 42, 15228-15235 (2007)